Computer Methods and Programs in Biomedicine 216 (2022) 106653

Contents lists available at ScienceDirect

Computer Methods and Programs in Biomedicine

journal homepage: www.elsevier.com/locate/cmpb

Development of a numerical multi-layer model of skin subjected to pulsed laser irradiation to optimise thermal stimulation in photorejuvenation procedure

Muhammad Muddassir[a,*], Georges Limbert[b,c], David Navarro-Alarcon[a]

[a] Department of Mechanical Engineering, The Hong Kong Polytechnic University (PolyU), KLN, Hong Kong
[b] Department of Mechanical Engineering, Faculty of Engineering and Physical Sciences, University of Southampton, Southampton, UK
[c] Department of Human Biology, Faculty of Health Sciences, University of Cape Town, Observatory 7935, South Africa

ARTICLE INFO

Article history:
Received 14 September 2021
Revised 10 December 2021
Accepted 20 January 2022

Keywords:
Skin photorejuvenation
Cosmetic dermatology
Robotics
Laser
Thermal interaction
Biophysics

ABSTRACT

Background and Objective: This paper presents the development of a 3D physics-based numerical model of skin capable of representing the laser-skin photo-thermal interactions occurring in skin photorejuvenation treatment procedures. The aim of this model was to provide a rational and quantitative basis to control and predict temperature distribution within the layered structure of skin. Ultimately, this mathematical and numerical modelling platform will guide the design of an automatic robotic controller to precisely regulate skin temperature at desired depths and for specific durations. Methods: The Pennes bioheat equation was used to account for heat transfer in a 3D multi-layer model of skin. The effects of blood perfusion, skin pigmentation and various convection conditions are also incorporated in the proposed model. The photo-thermal effect due to pulsed laser light on skin is computed using light diffusion theory. The physics-based constitutive model was numerically implemented using a combination of finite volume and finite difference techniques. Direct sensitivity routines were also implemented to assess the influence of constitutive parameters on temperature. A stability analysis of the numerical model was conducted. Results: Finally, the numerical model was exploited to assess its ability to predict temperature distribution and thermal damage via a multi-parametric study which accounted for a wide array of biophysical parameters such as light coefficients of absorption for individual skin layers and melanin levels (correlated with ethnicity). It was shown how critical is the link between melanin content, laser light characteristics and potential thermal damage to skin. Conclusions: The developed photo-thermal model of skin-laser interactions paves the way for the design of an automated simulation-driven photorejuvenation robot, thus alleviating the need for inconsistent and error-prone human operators.

1. Introduction

Skin photorejuvenation is a cosmetic treatment procedure in which a pulsed laser beam is irradiated over the skin surface to treat the effects of photo-ageing, wrinkles and pigmentation disorders. This technique is also increasingly used for hair and tattoo removal [1,2]. The spectrum of light used in this treatment ranges from infrared to ultraviolet [3–5]. Different types of treatments utilise a single (monochromatic) or multiple wavelengths (polychromatic) of laser light from this spectrum. The recovery time (down time) and the risk of post-treatment injury is minimal when using laser wavelengths within the infrared spectrum compared to those spanning the ultraviolet spectrum. This is primarily due to the composition of skin tissue: the ratio of water and lipids is higher than that of other constituents, especially in the dermis and hypodermis. Water and adipose tissue tend to absorb more light energy in the infrared spectrum than in the ultraviolet one.

At present, most dermatology clinics performing photorejuvenation treatment procedures use monochromatic or polychromatic laser lights emitting in the near-infrared (NIR) to infrared (IR) spectrum (500–1500 nm) [6,7]. Er:YAG 2940 nm and CO_2 10,0600 nm lasers are mostly utilised for the treatment of the effects of photo-ageing but they are more ablative as compared to the laser lights whose spectrum lies within the 500–1500 nm range. Photorejuvenation procedures based on these two laser lights induce deeper tissue injury and damage to the the epidermal layer which leads to longer healing time. For skin photorejuvenation, Nd:YAG 1064 nm

* Corresponding author.
E-mail addresses: mohammad.muddassir@connect.polyu.hk (M. Muddassir), g.limbert@soton.ac.uk (G. Limbert), dnavar@polyu.edu.hk (D. Navarro-Alarcon).

https://doi.org/10.1016/j.cmpb.2022.106653
0169-2607/

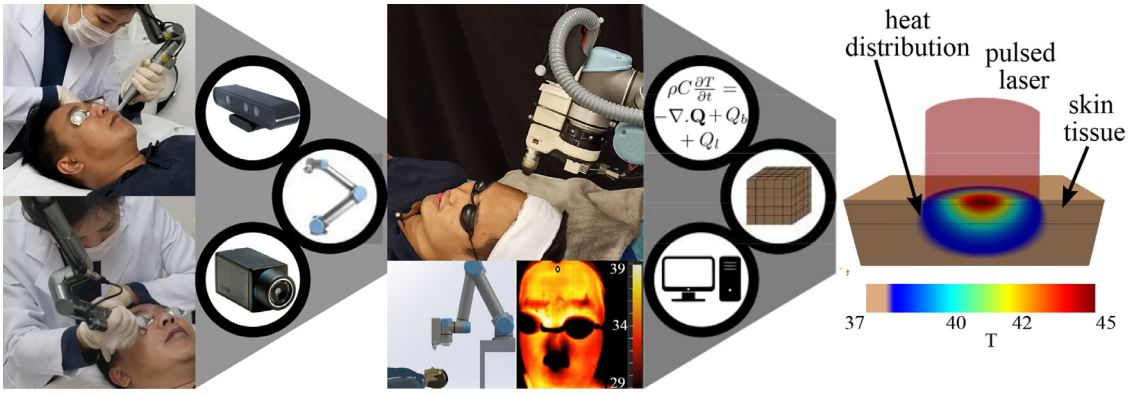

Fig. 1. Illustration of the concept of simulation-based controlled robot for laser photorejuvenation procedures. In a previous study [15,16], the introduction of sensors and robot manipulator automates treatment and improves the delivery of laser light irradiation on the skin.

near-infrared (NIR) laser provides a good trade-off between effectiveness of treatment and healing time, with less risk of post-treatment injury. Thermal stimulation of the dermis layer induces a controlled injury and denaturises collagen. This triggers a healing mechanism which promotes synthesis and remodelling of collagen [8–10]. Dams et al. [11,12] experimentally showed enhancement of collagen synthesis in the dermis in *in-vitro* and *ex-vivo* human skin by rising temperature to 45°C. From the therapeutic point of view, a temperature rise to up to 45°C in the dermis does not compromise the viability of dermal tissue and can improve the appearance of the treated skin.

In the context of a skin photorejuvenation procedure, before irradiating the laser light over the skin surface, a physician or trained technician selects the most appropriate laser settings based on their expertise and experience, These settings include laser beam diameter, laser energy and fluence (energy per unit area) [13,14]. Moreover, laser irradiation should be distributed uniformly over the treated area for better aesthetic outcome. Typically, the operator decides heuristically on the number of repetitions of laser irradiation on the same area to achieve an optimal degree of thermal stimulation in the dermis. This layer lies few hundred micrometres beneath the skin surface and, as consequence, precisely regulating its spatial temperature distribution remains challenging. It is clear that such a subjective and human-centred approach cannot ensure consistency of results as it lacks a rational and quantitative basis to predict the amount of thermal stimulation required, particularly if one aims to account for patient-specific skin biophysical properties, in addition to the inability to consistently and precisely apply the laser beam at specific locations and for specified durations.

Previous studies [15,16] have reported a novel skin photorejuvenation robot that can irradiate the laser light uniformly and that has enabled the automation of the treatment to some degree. However, despite this robot significantly improving the delivery of laser irradiation in terms of spatial accuracy, it lacks the capabilities to estimate and predict the amount of thermal stimulation needed so that specific temperature distributions could be obtained at critical locations within the dermal tissue. Such a technological capability constitutes the next step in our engineering development and is the object of the study presented in the current paper. The concept of automated simulation-driven skin photorejuvenation robot is illustrated in Fig. 1. The objective of our study is to develop a three-dimensional multiphysic numerical multi-layer model of skin subjected to pulsed 1064 nm laser light in order to analyse its photo-thermal response.

This numerical model accounts for temporal and spatial distribution of temperature in each skin's individual layers whilst considering the thermal effect of blood perfusion, external cooling conditions and a wide range of skin constituents' biophysical properties such as coefficient of light absorption and melanin concentration. The model is also parametrised by laser light characteristics including wavelength, laser beam diameter, laser energy and fluence rate. The numerical model is based on the Pennes bioheat equation [17] and numerically approximated using the finite volume method (FVM) in the spatial domain. Then this numerical model is incrementally solved in the temporal domain using a four-stage Runge-Kutta method (RK4). A stability analysis of the RK4 method was conducted and provided upper bounds for the stable time step above which numerical convergence is no longer guaranteed. To evaluate the influence of model parameters on the output responses, namely temperature magnitude and distributions, direct sensitivity analyses were performed. The potential thermally-induced damage inflicted on the skin due to laser irradiation was also estimated.

The novel contributions of this study are as follows:

1. Constitutive formulation of a photo-thermal three-dimensional multi-layer model of skin which accounts for skin biophysical parameters and external parameters such as external temperature and laser light characteristics.
2. Analysis of the stability of the numerical model.
3. Parametric evaluation of the numerical model under a wide range of conditions and for diverse biophysical properties, and evaluation of temperature sensitivities against simulation parameters.
4. Development of a conceptual controller to regulate skin temperature at specific depth.

The rest of the manuscript is organised as follows: Section 2 presents the photo-thermal constitutive formulation of dermal tissue. Section 3 introduces the discretisation and solving techniques of the mathematical model. Section 4 reports the results obtained from simulation of various clinically realistic cases. Finally, conclusive remarks are provided in Section 6.

2. Mathematical modelling

2.1. Skin multi-layer bioheat model

Human skin tissue consists of three main layers, epidermis, dermis and hypodermis (hypodermis is also known as the subcutaneous layer) [18]. Each of these layers is heterogenous and features a microstructure spanning multiple length scales [19]. Thus, each layer exhibits distinct physical properties, particularly in terms of thermal transfer (e.g. thermal conductivity and heat capacity) and light transmission and scattering. Light absorption and scattering govern the interaction of light with the different layers of skin.

In this study, we considered a monochromatic laser beam with a wavelength of 1064 nm. Upon irradiation of laser light on the skin surface, the skin constituents absorb a fraction of the incident laser energy. In turn, this energy absorption increases the kinetic energy of molecules leading to an increase in temperature This is known as photothermal effect. The Pennes bioheat model provides a mathematical basis to study the transient heat diffusion inside the tissue. The modified Pennes model is described by the following equation [20] (The classical Pennes bioheat equation was reported in cylindrical coordinates, whereas we have used Cartesian coordinates here.):

$$\rho C \frac{\partial T}{\partial t} = -\nabla Q + Q_b + Q_l \tag{1}$$

Here, Q defines heat conduction and can be defined in terms of temperature as $k\nabla^2 T(\mathbf{r}, t))$ (k is the thermal conductivity of the tissue [W/(m$^2 \cdot$ K)], $\mathbf{r}$ is the position vector in Cartesian coordinates [m] and t is time [s].). ρ is the density of the tissue [kg/m^3], C the thermal capacity of the tissue [J/(Kg $\cdot$ K)], T the temperature of the tissue [K], ∇ the gradient operator, Q_b the volumetric heat loss due to blood perfusion, and Q_l the volumetric heat source due to light diffusion within the tissue [W/m^3].

2.2. Spatial diffusion of light in skin

The volumetric heat source Q_l depends on three components: light absorptivity of skin, local fluence rate and time function.

$$Q_l = \mu_a \ \Phi(\mathbf{r}) \ h(t) \tag{2}$$

where μ_a is the absorption coefficient [m^{-1}], which varies for different skin layers and light wavelengths. $\Phi(\mathbf{r})$ is the local fluence rate [W/m^2] or a distribution profile of light inside the skin tissue. $h(t)$ is a time function that controls the rate of irradiation and it will be discussed in Section 3.4.

Besides the extracellular matrix, human skin is composed of various living cells, chromophores and water molecules. Considering the absorption coefficient of each layer-specific material according to its volume fraction provides a more realistic approximation of the optical properties of the multi-layer tissue composite (i.e. skin). Here, the absorption coefficient of the skin is assumed to be a linearly weighted sum of the absorption coefficient of each of its layers [21].

$$\mu_a = \Sigma_i f_{v,i} \mu_{a,i} + (1 - \Sigma_i f_{v,i}) \mu_{a,0} \tag{3}$$

where $f_{v,i}$ denotes volume fraction (%) of the ith constituent of the tissue, and $\mu_{a,i}$ is the absorption coefficient of the ith constituent. $\mu_{a,0}$ is the baseline absorption coefficient. The absorption coefficient of the epidermis can be approximated by a linearly weighted sum of each constituent having relatively larger volume fractions:

$$\mu_{a,e} = f_{v,m} \mu_{a,m} + (1 - f_{v,m}) \mu_{a,e0} \tag{4}$$

where $\mu_{a,e}$ denotes the absorption coefficient of the epidermis, $f_{v,m}$ the volume fraction of melanin in the epidermis, and $\mu_{a,m}$ the absorption coefficient of melanin. $\mu_{a,m}$ is computed as follows [21]:

$$\mu_{a,m} = 6.6 \times 10^{13} \left(\frac{\lambda}{\text{nm}} \right)^{-3.33} \tag{5}$$

Here, λ is the wavelength of the irradiated laser light in nm. Melanin concentration in human skin defines skin complexion. A dark skin has a higher melanin content than a fair skin. Like many other researchers, Alaluf et al. [22,23] experimentally showed that skin complexion in various ethnicities is correlated with melanin content. In their comprehensive study, these authors have examined melanin content and composition across a range of major ethnic groups (European, Chinese, Mexican, Indian and African). It was shown that darker skin contains relatively more melanin and features larger melanosomes than lighter skin. Therefore, it is legitimate to use $f_{v,m}$ as a surrogate optical property correlated to a particular skin type. $\mu_{a,e0}$ is the baseline absorption coefficient and is defined as follows [21]:

$$\mu_{a,0} = 0.244 + 85.3 \exp(-\frac{\lambda - 154}{66.2}) \tag{6}$$

The absorption coefficient of the dermis significantly depends on the absorption coefficients of water and blood, as most blood vessels are located within the dermis. Thus, the dermal absorption coefficient is defined as

$$\mu_{a,d} = f_{v,b} \mu_{a,b} + f_{v,w} \mu_{a,w} + (1 - f_{v,b} - f_{v,w}) \mu_{a,0}. \tag{7}$$

Here, $\mu_{a,d}$ is the absorption coefficient of the dermis, $f_{v,b}$ is the volume fraction of blood in skin (i.e. as a composite multi-layer assembly), $\mu_{a,b}$ is the absorption coefficient of blood, $f_{v,w}$ is the volume fraction of the water content inside the dermis, and $\mu_{a,w}$ is the absorption coefficient of water. The absorption coefficient of blood highly depends on the concentration of oxygen in the blood. Thus, the absorption coefficient of blood can be represented as a linearly weighted sum of the absorption coefficient of oxygenated and deoxygenated blood:

$$\mu_{a,b} = sO_2 \mu_{a,oxy} + (1 - sO_2) \mu_{a,doxy}. \tag{8}$$

sO_2 defines the percentage of oxygen saturation in the blood, μ_{oxy} is the absorption coefficient of oxygenated blood, and μ_{doxy} is the absorption coefficient of deoxygenated blood. For macroscopic heat analysis, considering the absorption coefficient weighted by the volume fraction of the dominant chromophores of materials provides a better approximation of the absorption coefficient for the entire layer.

When the wavelength of laser light lies between 300 and 1000 nm, the scattering in non-pigmented tissue is greater than the absorption [3,24]. Then, the local fluence rate is defined as the sum of light distribution due to scattering and absorption in a scattering medium:

$$\Phi(\mathbf{r}) = \Phi_c(\mathbf{r}) + \Phi_d(\mathbf{r}) \tag{9}$$

Here, $\Phi_c(x, y, z)$ defines the attenuation of the collimated laser light due to absorption. $\Phi_d(x, y, z)$ is the light distribution due to scattering of photons in the scattering medium. x, y and z are the Cartesian position coordinates. $\Phi_c(\mathbf{r})$ is defined as

$$\Phi_c(\mathbf{r}) = I_o(1 - r_{sp}) I_r(x, y) I_b(z) \tag{10}$$

where the attenuation in the z-axis is defined by the Beer-Lambert law of coaxial attenuation $I_b(z) = \exp(-\mu_a + (1 - g)\mu_s(z - z_0))$, and the radial profile of the incident light source follows a Gaussian distribution $I_r(x, y) = \exp(-\{(x - x_0)^2 + (y - y_0)^2\}/\text{W})$. I_o is the incident irradiance [W/m$_2$], which depends on the power of the incident laser$P$ [W] and the waist of laser beam $w[m]$, $I_o = 2P/(\pi \text{W}^2)$. r_{sp} denotes the specular reflection of the skin surface. The laser power in terms of laser energy can be defined as $P = E/\tau$, where τ is the pulse duration [s]. y_0 and z_0 are the centre point of incident light. μ_s is the scattering coefficient, where g is the anisotropic factor. $I_r(x, y)$ defines the distribution of the incident laser light in skin tissue (Table 1).

Upon laser irradiation on skin tissue, a significant part of the irradiated laser light is scattered in the tissue, and an r_{sp} amount of laser light is reflected back. The light distribution inside the skin tissue due to scattering is defined using light diffusion theory [3,24,25]:

$$\nabla^2 \Phi_d(\mathbf{r}) - 3\mu_a[\mu_a + (1 - g)\mu_s]\Phi_d(\mathbf{r}) = -3\mu_s[\mu_s + (1 - g)\mu_a]\Phi_c(\mathbf{r}) \tag{11}$$

The scattering coefficient of a medium depends on the wavelength like the absorption coefficient and can be computed using the reduced scattering coefficient as follows [21]:

$$\mu_s^{'}(\lambda) = a^{'}\left(f_{Ray}\left(\frac{\lambda}{500}\right)^{-4} + \left(1 - f_{Ray}\right)\left(\frac{\lambda}{500}\right)^{-b_{Mie}}\right) \tag{12}$$

and $\mu_s^{'} = (1-g)\mu_s$. Here, f_{Ray} is the significance of the Rayleigh scattering, and $(1 - f_{Ray})$ is the Mie scattering at the reference wavelength. The parameters for each layer are given in Table 2.

2.3. Heat sinks

Blood perfusion in the skin can be considered as a continuous heat sink that prevents abrupt changes in tissue temperature. The continuous blood perfusion in the dermis is defined as [26,27]

$$Q_b = F\omega_b C_b(T_a - T). \tag{13}$$

Here, ω_b [kg/m^3 · s] is the rate of blood perfusion in the tissue, C_b [J/(kg · K)] is the specific heat of the blood, and T_a is the arterial temperature. F is a temperature-dependent scaling factor and is calculated as [27,28]

$$F = \begin{cases} 1 + a\exp(-\frac{(T-T_f)^2}{\omega}), & T \le T_F \\ 1 + a, & \text{otherwise} \end{cases} \tag{14}$$

Here, a is a scaling factor, ω controls the steepness of F, and T_F is the temperature where the maximum perfusion occurs. Song et al. [64] showed experimentally that the response of vascular systems is highly dependent on temperature variations and the maximum blood perfusion in a tissue occurs at 45°C. The values of these parameters are given in Table 2.

2.4. Natural and forced cooling

The convective interaction of the skin and air is formulated in the boundary condition of (1). At $z = 0$,

$$k\nabla_x T_{(z=0)} = h(T_0 - T), \quad T_{(z=0)} = T_0 \tag{15}$$

where h is the convection coefficient of air and T_0 is the ambient temperature. The other boundary conditions of the tissue are considered to be symmetric; that is,

$$k\nabla_x T_{(x=0,X)} = 0, \qquad T_{(x=0,X)} = T_a \tag{16}$$

$$k\nabla_y T_{(y=0,Y)} = 0, \qquad T_{(y=0,Y)} = T_a \tag{17}$$

$$k\nabla_z T_{(z=Z)} = 0, \qquad T_{(z=Z)} = T_a \tag{18}$$

and $T = T_a$ at $z = Z, x = 0, x = X, y = 0$ and $y = Y$ where the initial condition is $T|_{t=0} = T_a$. Fig. 2 shows the simulation domain under laser irradiation and convection.

3. Numerical methods

3.1. Spatio-temporal discretisation of bioheat equation

Eq. (1) is a general expression to compute the transient temperature in the skin while considering laser irradiance on the skin surface with blood perfusion in the tissue. To compute the temperature distribution in the skin, (1) is numerically integrated over a control volume, this method is known as finite volume method (FVM) or control volume method. Integrating (1) over a control volume (CV) yields:

$$\int_{CV} \rho C\frac{\partial T}{\partial t}\, dV = -\int_{CV} \nabla.Q\, dV + \int_{CV} Q_b\, dV + \int_{CV} Q_l\, dV \tag{19}$$

Applying the Green-Gauss-Ostrogradsky theorem [29,30] to expression $-\int_{CV} \nabla Q\, dV$ yields

$$-\int_{CV} \nabla.Q\, dV = -\int_{CS} Q.\mathbf{n}_s\, dS. \tag{20}$$

where CS is the control surface and $\mathbf{n}_s$ is the outward-pointing unit vector normal to the surface. As $Q.\mathbf{n}_s = 1.|Q|\cos(\mathbf{n}_s, Q)$, the direction of heat flows Q toward the control volume from the neighbouring control volumes and the direction of the surface normal $\mathbf{n}_s$ are opposite to each other, as shown in Fig. 2(b). The opposing direction of both vectors yields a negative scalar product. The computational domain is described in Cartesian coordinates, so the control volume is cuboidal, and each control volume is computed as $\Delta V = \Delta x\Delta y\Delta z$, where Δx, Δy and Δz are the spatial discretisation steps in the $x-$, $y-$ and $z-$axis, respectively. Then, (19) can be approximated as

$$\Delta V\rho C\frac{\partial T}{\partial t} = \Sigma_i Q_i + \Delta V Q_b + \Delta V Q_l \tag{21}$$

where Q_i is heat flux induced from the neighbouring control volumes, as shown in Fig. 2(b). $\Sigma_i Q_i$ is defined as

$$\Sigma_i Q_i = Q_{i,j+1,k} + Q_{i,j-1,k} + Q_{i+1,j,k} + Q_{i-1,j,k} + Q_{i,j,k+1} + Q_{i,j,k-1}. \tag{22}$$

Fig. 3(a) and (b) shows the spatial discretised domain assumed in this article. The coordinate system of the domain in Fig. 3 mimics the structure of a three-dimensional matrix, where columns is along the x-axis, rows is along the y-axis and depth is along the z-axis Thus, each control volume will be referenced via their index number i, j and k in the domain; that is i will increase in the y-axis (rows), k in the x-axis (columns) and j in the z-axis (depth). Now, the heat flux flowing from the neighbouring control volume is calculated as [29],

$$Q_{i,j+1,k} = \Delta y\Delta z\ \frac{k_{i,j+1,k} + k_{i,j,k}}{2}\ \frac{T_{i,j+1,k} - T_{i,j,k}}{\Delta x} \tag{23}$$

$$Q_{i,j-1,k} = \Delta y\Delta z\ \frac{k_{i,j-1,k} + k_{i,j,k}}{2}\ \frac{T_{i,j-1,k} - T_{i,j,k}}{\Delta x} \tag{24}$$

$$Q_{i+1,j,k} = \Delta z\Delta x\ \frac{k_{i+1,j,k} + k_{i,j,k}}{2}\ \frac{T_{i+1,j,k} - T_{i,j,k}}{\Delta y} \tag{25}$$

$$Q_{i-1,j,k} = \Delta z\Delta x\ \frac{k_{i-1,j,k} + k_{i,j,k}}{2}\ \frac{T_{i-1,j,k} - T_{i,j,k}}{\Delta y} \tag{26}$$

$$Q_{i,j,k+1} = \Delta x\Delta y\ \frac{k_{i,j,k+1} + k_{i,j,k}}{2}\ \frac{T_{i,j,k+1} - T_{i,j,k}}{\Delta z} \tag{27}$$

$$Q_{i,j,k-1} = \Delta x\Delta y\ \frac{k_{i,j,k-1} + k_{i,j,k}}{2}\ \frac{T_{i,j,k-1} - T_{i,j,k}}{\Delta z} \tag{28}$$

where k and T without any subscript are associated with the control volume considered while those with subscripts are the neighbouring control volumes. The thermal conductivity of control volumes in the xy-plane is constant as change of layer only occurs along the direction of the z-axis, so $k = k_{i,j+1,k} = k_{i,j-1,k} = k_{i+1,j,k} = k_{i+1,j,k}$. Now, dividing (19) by $\Delta x\Delta y\Delta z\rho C$ and plugging (23) back to (19) yields:

$$\begin{aligned}\frac{\partial T_{i,j,k}}{\partial t} = &\frac{k}{\rho C\Delta y^2}\left(T_{i+1,j,k} + T_{i-1,j,k}\right) \\ &+ \frac{k}{\rho C\Delta x^2}\left(T_{i,j+1,k} + T_{i,j+1,k}\right) \\ &+ \frac{1}{\rho C\Delta z^2}\left[\frac{k_{k+1} + k}{2}.T_{i,j,k+1} + \frac{k_{k-1} + k}{2}.T_{T_{i,j,k-1}}\right]\end{aligned}$$

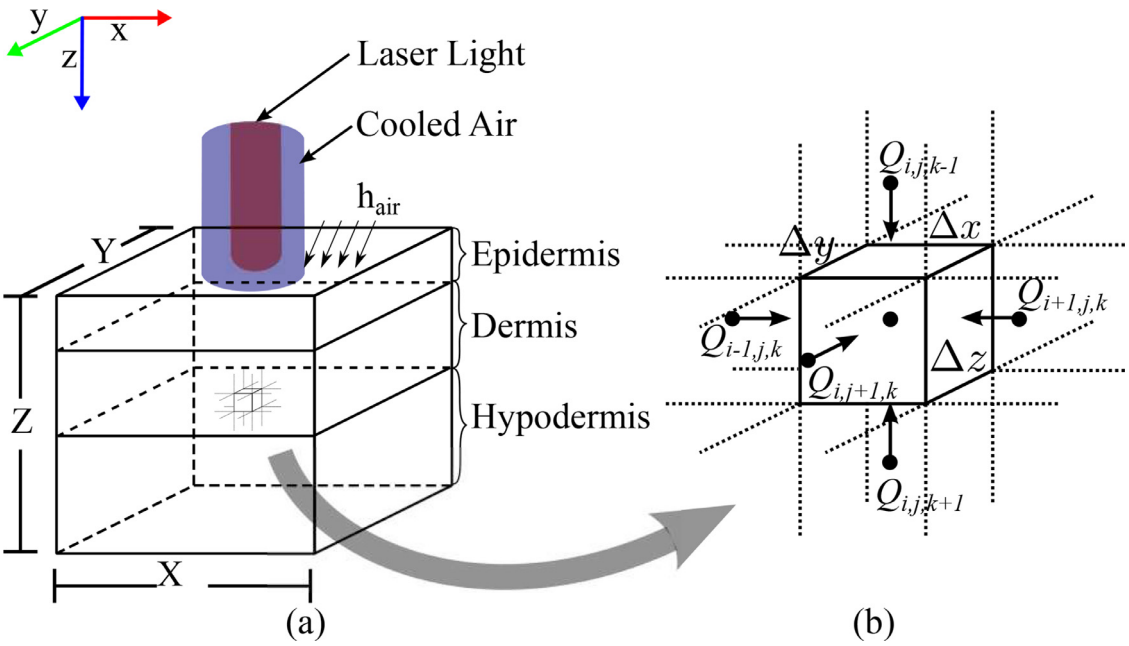

Fig. 2. Computational domain. (a) Simulated three-layered skin tissue under laser light irradiation and forced air cooling. (b) Flow of heat flux from the neighbouring control volumes.

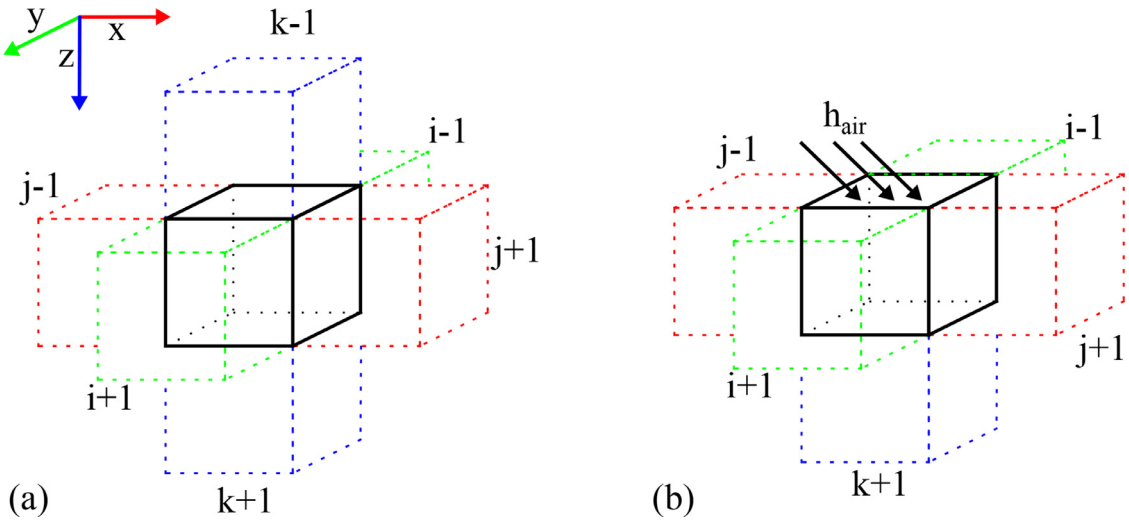

Fig. 3. Control volume. (a) Intermediate control volume. (b) Boundary control volume undergoing convection.

$$-\frac{1}{\rho C}\left(\frac{2k}{\Delta x^2}+\frac{2k}{\Delta y^2}+\frac{k_{k+1}+2k+k_{k-1}}{2\Delta z^2}+\omega_b C_b\right)T_{i,j,k} + \frac{1}{\rho C}T_a+\frac{1}{\rho C}Q_l \tag{29}$$

This expression can be simplified as follows:

$$\frac{\partial T_{i,j,k}}{\partial t} = -C_1 T_{i,j,k} + C_2. \tag{30}$$

Here, C_1 is the coefficient of $T_{i,j,k}$, and C_2 accounts for all the terms that are independent of $T_{i,j,k}$. The solution of this first-order differential equation can be approximated by the fourth-order Runge-Kutta numerical scheme. Then the approximate solution using explicit RK4 scheme will be:

$$T^{n+1}_{i,j,k} = T^{n}_{i,j,k} + \Delta t \Lambda \mathbf{b}^T \mathbf{Y} \tag{31}$$

Here, the superscript n denotes the current time in the discretised time domain, Δt is the time step, and $\mathbf{Y} = [K_1, K_2, K_3, K_4]^T$, where the K_i are the evaluation of (30) at ith stage of RK4 scheme. A is a matrix that defines the stages dependence on each other, and $\mathbf{b}$ is the weight given to each stage during the final evaluation. The approximate solution at the four stages of the RK4 scheme is computed by

$$\mathbf{Y} = \mathbf{1}T^{n}_{i,j,k} + \Delta t \Lambda \mathbf{A}\mathbf{Y} = (\mathbf{I} - \Delta t \Lambda \mathbf{A})^{-1}\mathbf{1}T^{n}_{i,j,k}. \tag{32}$$

where the parameters $\mathbf{A}$, $\mathbf{b}$ and $\mathbf{c}$ are derived from the Butcher's tableau for the RK41 scheme [31], and $\mathbf{1}$ is a 4×1 vector of ones.

3.2. Numerical solution of light diffusion equation

Eq. (11) is in the form of a standard diffusion equation and is numerically solved using the FVM. Integrating (11) over a control volume and assuming that $\Phi_d(x, y, z) = \Phi_d$ and $\Phi_c(x, y, z) = \Phi_c$,

$$\int_{cv} \nabla^2 \Phi_d dv \quad - \int_{cv} 3\mu_a[\mu_a + (1-g)\mu_s]\Phi_d dv = - \int_{cv} 3\mu_s[\mu_s + (1+g)\mu_a]\Phi_c dv. \tag{33}$$

Applying the Green-Gauss-Ostrogradsky theorem on the term $\int_{cv} \nabla^2 \Phi_d dv$ gives,

$$\int_{cv} \nabla(\nabla \Phi_d) dv = \int_{cs} \nabla(\nabla \Phi_d).\mathbf{n} ds \tag{34}$$

Thus, the scalar product in the equation allows only the flux to be non-zero, which is normal to the face of each side.

$$\int_{cs} \nabla(\nabla \Phi_d).\mathbf{n}\ ds = A_E \left(\frac{\partial \Phi_d}{\partial x}\right)_E + A_W \left(\frac{\partial \Phi_d}{\partial x}\right)_W + A_N \left(\frac{\partial \Phi_d}{\partial y}\right)_N + A_S \left(\frac{\partial \Phi_d}{\partial y}\right)_S + A_U \left(\frac{\partial \Phi_d}{\partial z}\right)_U + A_D \left(\frac{\partial \Phi_d}{\partial z}\right)_D \tag{35}$$

Then, the Taylor expansion of each partial derivative will be

$$\begin{aligned} &\int_{cs} \nabla(\nabla \Phi_d).\mathbf{n}\ ds \\ &= A_E \frac{\Phi_{d,E} - \Phi_d}{\Delta x} + A_W \frac{\Phi_{d,W} - \Phi_d}{\Delta x} + A_N \frac{\Phi_{d,N} - \Phi_d}{\Delta y} \\ &\quad + A_S \frac{\Phi_{d,S} - \Phi_d}{\Delta y} + A_U \frac{\Phi_{d,U} - \Phi_d}{\Delta z} + A_D \frac{\Phi_{d,D} - \Phi_d}{\Delta z}. \end{aligned}$$

Where $A_E = \Delta y \Delta z$, $A_W = \Delta y \Delta z$, $A_N = \Delta z \Delta x$, $A_S = \Delta z \Delta x$, $A_U = \Delta x \Delta y$ and $A_D = \Delta x \Delta y$ are the interfacing areas between two control volumes. Now substituting it back to (33) gives

$$\begin{aligned} &A_E \frac{\Phi_{d,E} - \Phi_d}{\Delta x} + A_W \frac{\Phi_{d,W} - \Phi_d}{\Delta x} + A_N \frac{\Phi_{d,N} - \Phi_d}{\Delta y} \\ &\quad + A_S \frac{\Phi_{d,S} - \Phi_d}{\Delta y} + A_U \frac{\Phi_{d,U} - \Phi_d}{\Delta z} + A_D \frac{\Phi_{d,D} - \Phi_d}{\Delta z} \\ &\quad - 3\mu_a[\mu_a + (1-g)\mu_s]\Phi_d \Delta v \\ &= -3\mu_s[\mu_s + (1+g)\mu_a]\Phi_c \Delta v \end{aligned} \tag{36}$$

which further simplifies to

$$\begin{aligned} &\left[\frac{2}{\Delta x^2} + \frac{2}{\Delta y^2} + \frac{2}{\Delta z^2} + 3\mu_a\{\mu_a + (1-g)\mu_s\}\right]\Phi_d \\ &- \frac{1}{\Delta x^2}(\Phi_{d,E} + \Phi_{d,W}) - \frac{1}{\Delta y^2}(\Phi_{d,N} + \Phi_{d,S}) \\ &- \frac{1}{\Delta z^2}(\Phi_{d,U} + \Phi_{d,D}) = 3\mu_s[\mu_s + (1+g)\mu_a]\Phi_c. \end{aligned}$$

An iterative linear equation solver (GMRES) was utilised to solve this system of linear equations. The complete simulation domain consists of a uniform tissue, and the light source will always irradiate on $z = 0$. Thus, the distribution of light scattering inside the tissue is translation-invariant in the x and y-axis. The iterative methods to solve systems of linear equations are relatively slow but efficient in term of computer memory management. The scattering of light distribution is only determined at the start of the simulation and reused for the later time steps of irradiation.

3.3. Stability analysis

To ensure that the numerical solution converges we performed a stability analysis of the model in (30). To find the region of stability, the stability function is derived by substituting (32) into (31):

$$T^{n+1}_{i,j,k} = T^n_{i,j,k} + \Delta t \Lambda \mathbf{b}^T (\mathbf{I} - \Delta t \Lambda \mathbf{A})^{-1} \mathbf{1} T^n_{i,j,k} \tag{37}$$

$$T^{n+1}_{i,j,k} = (1 + \Delta t \Lambda \mathbf{b}^T (\mathbf{I} - \Delta t \Lambda \mathbf{A})^{-1} \mathbf{1}) T^n_{i,j,k} \tag{38}$$

Let $\gamma = \Delta t \Lambda, \gamma \in \mathbb{C}$. Then the stability function will be [31]

$$R(\gamma) = 1 + \Delta t \Lambda \mathbf{b}^T (\mathbf{I} - \gamma \mathbf{A})^{-1} \mathbf{1}. \tag{39}$$

Now expanding the $((\mathbf{I} - \gamma \mathbf{A})^{-1})$ using binomial series yields

$$R(\gamma) = 1 + \gamma \mathbf{b}^T \mathbf{1} + \gamma^2 \mathbf{b}^T \mathbf{A} \mathbf{1} + \gamma^3 \mathbf{b}^T \mathbf{A}^2 \mathbf{1} + \gamma^4 \mathbf{b}^T \mathbf{A}^3 \mathbf{1} + \cdots. \tag{40}$$

The explicit method holds an order condition, that is $\mathbf{b}^T \mathbf{A}^l \mathbf{1} = \mathbf{b}^T \mathbf{A}^{l-1} \mathbf{c}$ where $l = 1, 2, 3, \ldots$ Applying this condition gives,

$$R(\gamma) = 1 + \gamma \mathbf{b}^T \mathbf{1} + \gamma^2 \mathbf{b}^T \mathbf{A}^0 \mathbf{c} + \gamma^3 \mathbf{b}^T \mathbf{A} \mathbf{c} + \gamma^4 \mathbf{b}^T \mathbf{A}^2 \mathbf{c} + \cdots. \tag{41}$$

The coefficients of γ become zero when the order of γ becomes greater than the number of stages in RK4 scheme [31]. Thus, the series in (41) will be left until the fourth order. Then, the stability criteria of the numerical scheme are stable when $|R(\gamma)| < 1$ or

$$-1 < 1 + \gamma \mathbf{b}^T \mathbf{1} + \gamma^2 \mathbf{b}^T \mathbf{A} \mathbf{1} + \gamma^3 \mathbf{b}^T \mathbf{A}^2 \mathbf{1} + \gamma^4 \mathbf{b}^T \mathbf{A}^3 \mathbf{1} < 1. \tag{42}$$

Fig. 4 shows the region of stability at each stage of RK4 scheme. To compute the upper bound of the time step Δt, (42) is factorised. Then, the smallest real positive root is the upper bound of h. A time step greater than this value will lead to divergence of the numerical solution.

3.4. Automatic thermal regulation

The main reason to compute the heat distribution inside the skin is to enable the photorejuvenation robot, reported in [15,16], to regulate and/or maintain a desired temperature at a specific depth within the skin. Thus, defining a control law will ensure optimal temperature regulation. Let (30) be a dynamic system of control volume in a simulation domain and represent a system. With some simplifications in (30),

$$\dot{T}(t) = -C_1 T(t) + C_3 + C_4 h(t) \tag{43}$$

where the $C_2 = C_3 + C_4 h(t)$. C_3 is the heat gain/loss due to neighbouring control volumes and the volumetric heat source/sink, and C_2 is the contribution of each laser irradiation (i.e. input gain). Here, the input $h(t)$ can introduce the heat in the system but cannot withdraw it. $h(t)$ is a relay function that can switch states between 0 and 1, $0 \le h(t) \le 1$.

To regulate the temperature at the desired depth, a controller is designed which can reach the desired temperature in a minimum amount of time. The short pulsed nature of the laser irradiation justifies the design choice of impulse function as an input. Physical laser machines have a fixed minimum delay between each irradiation. If the time period between each laser irradiation is τ_{ir}, then the input $h(t, \tau_{ir})$ can be defined as a unit comb function (impulse train):

$$h(t) = \sum_{p=0}^{P} \{\delta(t - p\tau_{ir})\} \tag{44}$$

Here, $h(t)$ acts as an input to the system defined in (43) and p is an impulse index $p = 1, 2, 3, \ldots, P$. τ_{ir} is inversely proportional to the difference between the current state of system (43) and the desired state T_d. Thus,

$$\tau_{ir} = \begin{cases} \xi . T_e & T_e > 0 \\ 0 & T_e \le 0 \end{cases} \tag{45}$$

Here, $T_e = T(t) - T_d$, and ξ is a scaling factor. In practice, the laser equipment can irradiate only a pulsed laser after a minimum time period. In practice laser equipment has a limited rate of irradiation. Thus, $\tau_{ir,\min}$ is the minimum possible time step between two consecutive laser irradiations. Fig. 5 shows the controller output and evolution of the time period τ_{ir}. Fig. 6 depicts the schematic diagram of the control system used to regulate temperature.

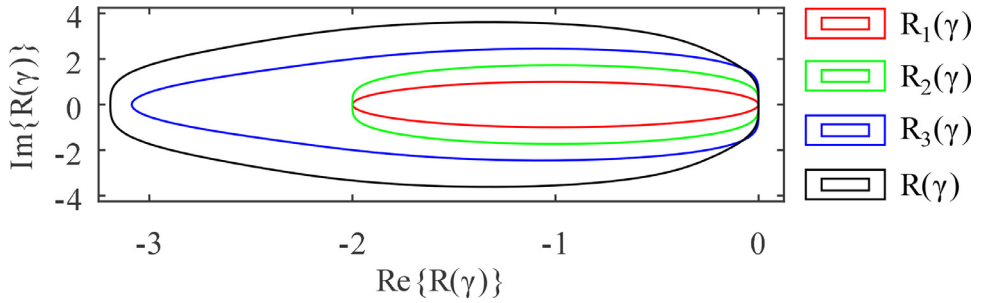

Fig. 4. Regions of stability at different stages of RK4 scheme. $R_1(\gamma)$, $R_2(\gamma)$, $R_3(\gamma)$ are the regions of stability for RK4 at each stage, where $R_1(\gamma) = 1 + \gamma \mathbf{b}^T\mathbf{1}$, $R_2(\gamma) = 1 + \gamma \mathbf{b}^T\mathbf{1} + \gamma^2 \mathbf{b}^T\mathbf{A}\mathbf{1}$, $R_3(\gamma) = 1 + \gamma \mathbf{b}^T\mathbf{1} + \gamma^2 \mathbf{b}^T\mathbf{A}\mathbf{1} + \gamma^3 \mathbf{b}^T\mathbf{A}^2\mathbf{1}$ and $R(\gamma) = 1 + \gamma \mathbf{b}^T\mathbf{1} + \gamma^2 \mathbf{b}^T\mathbf{A}\mathbf{1} + \gamma^3 \mathbf{b}^T\mathbf{A}^2\mathbf{1} + \gamma^4 \mathbf{b}^T\mathbf{A}^3\mathbf{1}$.

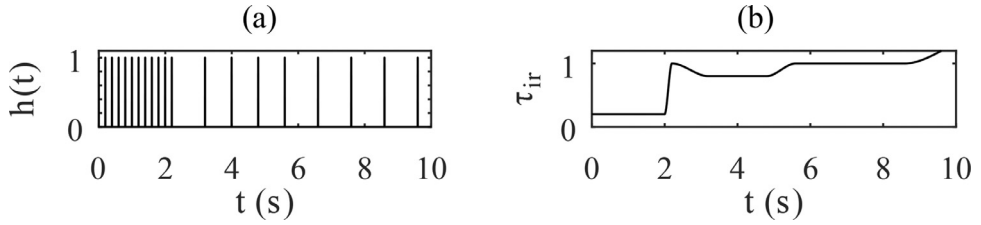

Fig. 5. Controller output of the automatic thermal regulation. For the plotted case, the melanin content in the skin was $f_{v,m} = 1\%$ and convection coefficient was $h = 10$ W/m$^2 \cdot$ K. Here $h(t)$ is the time function and τ_{ir} is the time period between each laser irradiation. (a) $h(t)$ with respect to time. The time period between each laser irradiation depends on the error between current and target temperature. (b) Evolution of time period τ_{ir} with respect to time. The minimum possible time period is $\tau_{ir,\min} > 0$, whereas the maximum is not bounded.

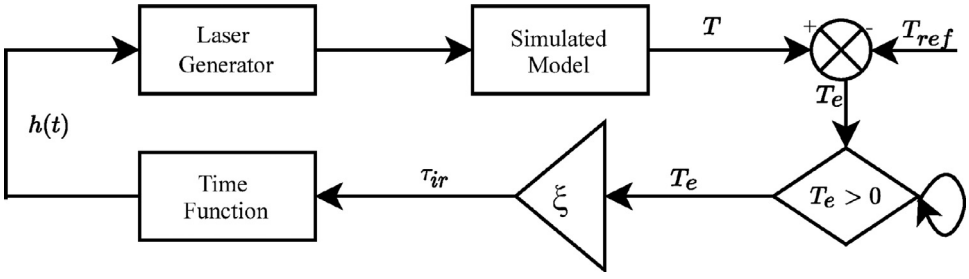

Fig. 6. Schematic diagram of the control system to regulate the desired temperature at the centre of epidermis-dermis interface.

Table 1
Range of the parameters in used sensitivity analysis.

	k(W/m.K)	μ_a (cm^{-1})	μ_s'(cm^{-1})	Δx(mm)	Δy(mm)	Δz(mm)
E	0.32–0.5	4.41–5.81	30–60.47	0.5–1	0.5–1	0.05–0.1
D	0.32–0.5	0.21–0.52	17.7–38.8	0.5–1	0.5–1	0.05–0.1
H	0.18–0.3	0.21–0.5	16.93–31.37	0.5–1	0.5–1	0.05–0.1

$h = 10 - 150$ W/m$^2 \cdot$ K. E, epidermis; D, dermis; H, hypodermis; k, thermal conductivity; μ_a, absorption coefficient; μ_s', reduced scattering coefficient; Δx, spatial resolution in x-axis; Δy, spatial resolution in y-axis; Δz, spatial resolution in z-axis.

4. Results

4.1. Sensitivity analysis

In order to assess the behaviour of the photo-thermal model of skin-laser interactions direct sensitivity routines were implemented using numerical differentiation [32,33]. A sensitivity analysis was performed to compute temperature sensitivities with respect to a range of physical and optical parameters of the skin, as reported in Table 1. The effect of spatial discretisation resolution over the simulation domain was also evaluated. The sensitivity vector is defined as

$$\boldsymbol{\zeta} = (k_e, k_d, k_h, h, \mu_{a,e}, \mu_{a,d}, \mu_{a,h}, \mu'_{s,e}, \mu'_{s,d}, \mu'_{s,h}, \Delta x, \Delta y, \Delta z)^T. \tag{46}$$

The sensitivity matrix can be defined as $\boldsymbol{\varphi} = \partial T(\boldsymbol{\zeta})/\partial \boldsymbol{\zeta}$. Each component of φ represents the rate of change of temperature as a result of a unit change in the corresponding parameter. The first four elements in φ are physical parameters, the last three are the spatial discretisation steps, and the remaining are the optical parameters of each skin layer. The domain of each parameter is defined from reported experimental values found in the literature. Hasgall et al. [34] provide a complete range of physical and optical parameters for human skin. To compute temperature sensitivities, a simulated skin domain with a size of $10 \times 10 \times 2.5$ mm^3 was considered (Fig. 6).It was composed of three layers: epidermis, dermis and hypodermis. The thickness of these layers were 0.5, 1 and 1 mm, respectively. Each layer had distinct physical and optical properties. The surface of the simulated skin sample was exposed to a 1064 nm pulsed laser light source of 1 J energy for 30 s. The laser source was positioned at the geometric centre of the skin sur-

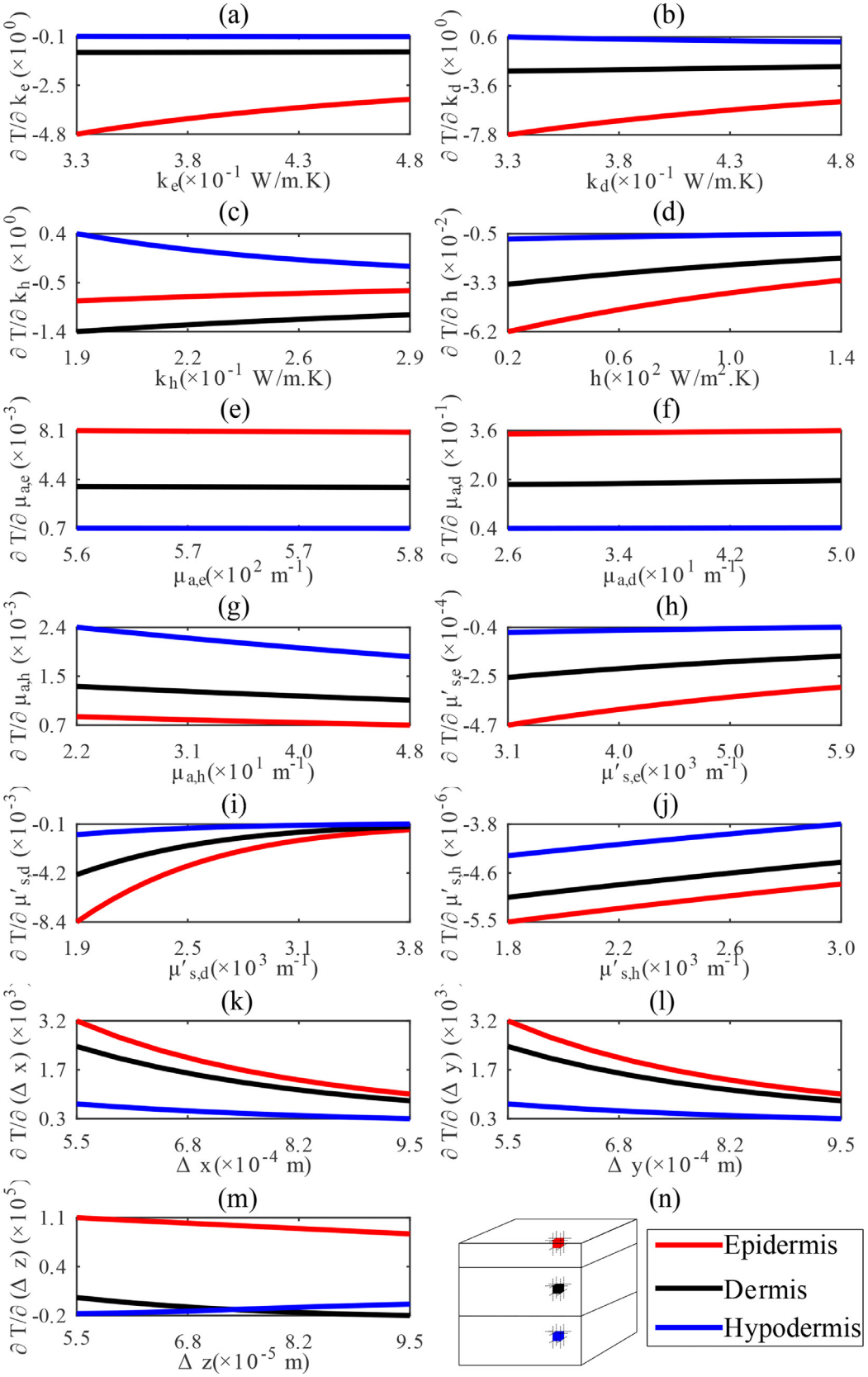

Fig. 7. Temperature sensitivities with respect to a subset of physical, optical parameters and spatial steps over a simulation domain. The plotted sensitivities are probed at the geometric centre of each layer. (a), (b) and (c) are the temperature sensitivities to the heat conductivity of the epidermis, dermis and hypodermis, respectively, whereas (d) is with respect to the convection heat coefficient. (e), (f) and (g) are the temperature sensitivities to the absorption coefficients of the epidermis, dermis and hypodermis, respectively. (h), (i) and (j) are temperature sensitivities with respect to reduced scattering of the epidermis, dermis and hypodermis, respectively. (k), (l) and (m) are temperature sensitivities to the spatial steps in *x*, *y* and *z*-axis, respectively. (n) the probes of the plotted sensitivities are in the geometric centre of each layer.

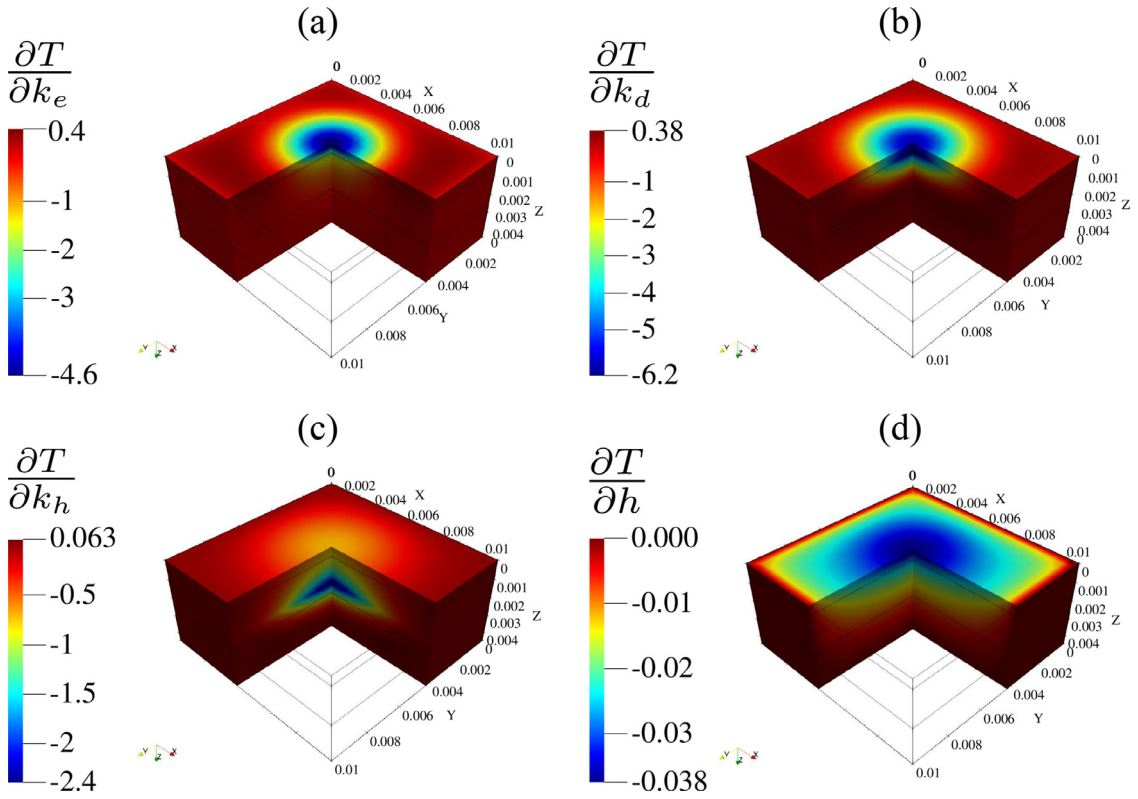

Fig. 8. Temperature sensitivities with respect to a subset of the physical parameters over the simulation domain. (a)–(c) are the temperature sensitivities with respect to heat conductivity of epidermis, dermis and hypodermis. (d) is temperature sensitivities respect to heat coefficient of convection. For the plotted coloured meshes, the values of heat conductivity of epidermis, dermis and hypodermis were 0.498 W/m · K and convection coefficient was 150 W/ · K.

face ($x = X/2$, $y = Y/2$ and $z = 0$). The duration of each laser pulse was 2 ms (or pulse width) repeating at a 10 Hz frequency whilst the waist of the laser light was 6 mm. Temperature sensitivities with respect to ζ were computed within each finite volume of the discretised domain. Fig. 7 shows the temperature sensitivities of a control volume located at the geometric centre of each layer.

Fig. 7 (a)–(c) shows the rate of temperature changes with respect to the heat conductivity coefficient for each layer. In Fig. 7(a) and (b), the trends are relatively similar and show no rapid temperature changes in the dermis and hypodermis, while changing the heat conductivity of the epidermis and dermis. However, the change in heat conductivity of epidermis and dermis increase the temperature sensitivity in the epidermis. Varying the thermal conductivity of the hypodermis influenced the thermal response of all three layers, as shown in Fig. 7(c). When applying different convection conditions, the temperature sensitivities decreased with increasing depth (Fig. 8(d)). Distributions of temperature sensitivities with respect to each physical parameter were mapped to the computational domain as shown in Fig. 8.

The temperature sensitivities with respect to the optical parameters of the skin tissue layers are shown in Fig. 7(e)–(j). The change in absorption coefficient of the epidermis ($\mu_{a,e}$) and dermis ($\mu_{a,d}$) exhibit no significant change in temperature sensitivities. Whereas the temperature change is more sensitive whistle varying absorption coefficient of the hypodermis ($\mu_{a,e}$). On the contrary, the change in reduced scattering coefficients of any layer influences the temperature change in whole simulated tissue.

To assess the varying optical parameters in the simulation domain, the temperature sensitivities for each control volume were mapped on the coloured meshes, as shown in Fig. 9. In Fig. 7 (l)–(n), the spatial steps show considerable influence over the temperature distribution in all layers. The change in the spatial step greatly affects the temperature trends in the epidermis. The small thickness of the epidermis compared with other skin layers is the reason for this behaviour. A mesh sensitivity analysis was not considered in the context of the direct parameter sensitivity analysis described above. The optimal grid size to obtain mesh convergence was determined in a preliminary study not reported here. The temperature sensitivities over the change in spatial step in the simulation domain are shown in Fig. 10 in the form of a sensitivity-mapped coloured mesh.

4.2. Controlled thermal stimulation

For that part of our numerical study, the dimensions of the three-layer skin structure were $2.5 \times 2.5 \times 0.75$ cm^3 while the thicknesses of the epidermis, dermis and hypodermis were 0.5, 2 and 5 mm, respectively. The thickness of the skin layers varies according to age, gender and body site. On that basis, averaged thickness values found in the literature [64–67] were used. The physical and optical properties of each layer are listed in Table 2. Here, we utilised the model of laser-skin interaction model described in Section 2 and 3 to regulate temperature at the epidermis-dermis interface. Heat regulation was achieved by controlling the time period between each laser irradiation (τ_{ir}). The skin was irradiated with a 1064 nm pulsed laser light source of 1.5 J covering a circular profile of 4 mm radius with a maximum repetition rate of 5 Hz. Photo-thermal laser-skin interactions were studied by considering two distinct convection conditions: ambient atmosphere (normal convection) and forced cooling. For normal convection, the ambient temperature of air was assumed to be $T_0 = 22^\circ$C, with a corresponding convection coefficient was $h = 10$ W/m^2 · K. This ambient air temperature and convection coefficient, T_0 and h respectively, are the same for the forced cooling case. More specifically, for the forced cooling cases, a short blow of 11°C air was puffed on

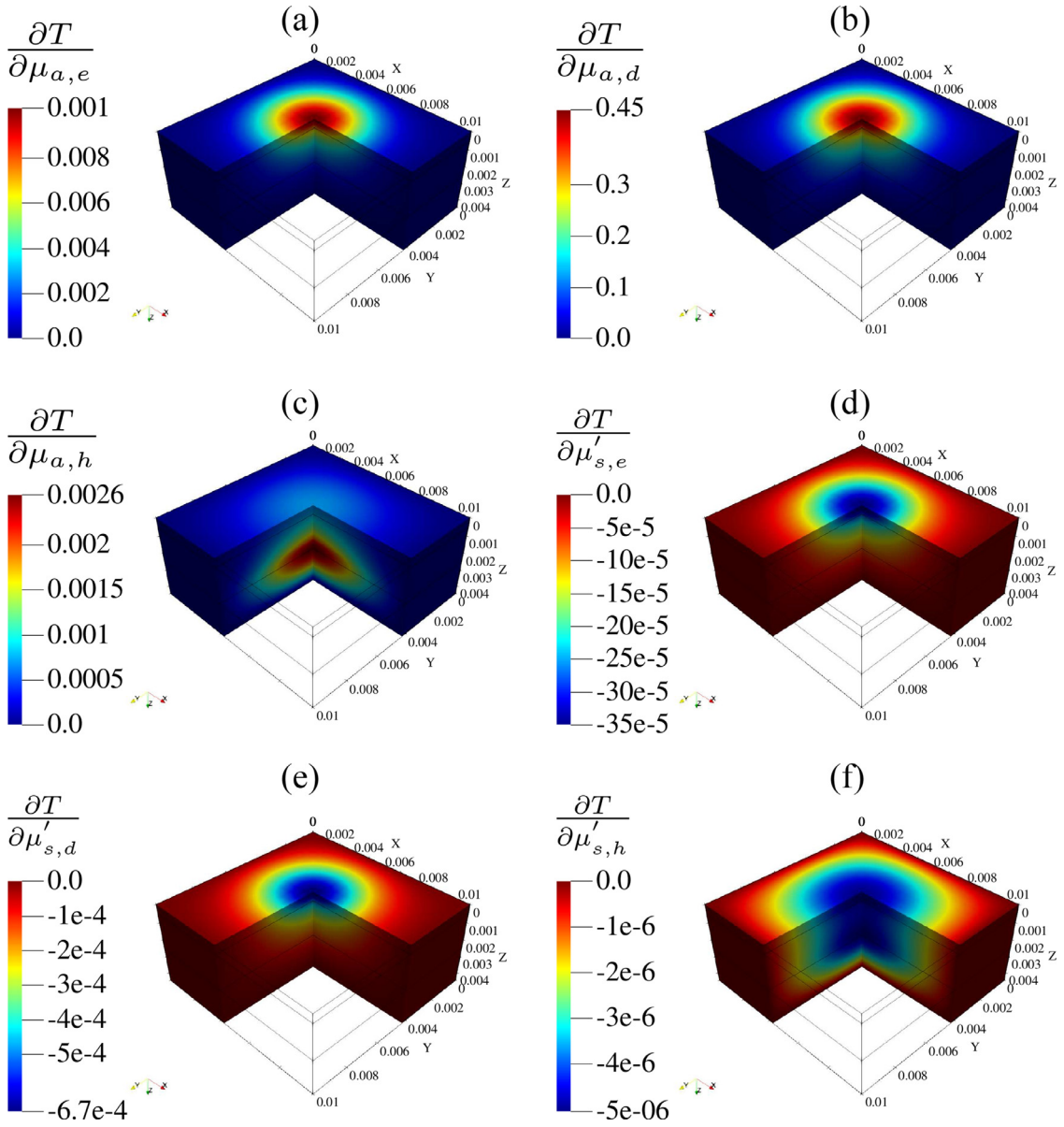

Fig. 9. Temperature sensitivities with respect to a subset of the optical parameters over the simulation domain. (a)–(c) are the temperature sensitivities with respect to absorption coefficient of epidermis (5.81 cm^{-1}), dermis (0.52 cm^{-1}) and hypodermis (0.5 cm^{-1}). (d)–(f) are temperature sensitivities respect to scattering coefficient of epidermis, dermis and hypodermis. Their values were respectively 60.47, 38.8 and 31.37 cm^{-1}.

Table 2
Physical and optical parameters of the simulated tissue in Section 3.4

	k(W/m.K)	ρ(Kg/m^3)	C(J/Kg.K)	T_a(^{0}C)	ω_b(Kg/m^3.s)	μ_a(cm^{-1})	$\mu_s^{'}$(cm^{-1})	$a^{'}$	f_{Ray}	b_{Mie}	r_{sp}	g
E	0.34	1120	3200	–	0	0.66/ 1.08/ 2.33/ 4.41	29.1	66.7	0.29	0.689	0.1	0.91
D	0.41	1090	3500	–	0.76	0.196	17.7	436.7	0.41	0.562	0.1	0.91
H	0.30	860	2870	–	0.22	0.21	16.93	34.2	0.26	0.567	0.1	0.91
B	–	1060	3770	37.4	–	3/1.88	–	–	–	–	–	–

E, epidermis; D, dermis; H, dermis; B, blood; k, thermal conductivity; C, thermal capacity; T_a, atrial temperature; ω_b, blood perfusion rate; μ_a, absorption coefficient; $\mu_s^{'}$, reduced scattering coefficient; f_{Ray}, fraction of Rayleigh scattering; b_{Mie}, fraction of Mie scattering; r_{sp}, specular reflection; g, anisotropy. μ_a of dermis are for 1, 2, 5 and 10%. μ_a of blood are for oxygenated and deoxygenated blood.

the skin surface for 75 ms during each laser irradiation. The convection coefficient of blown air was 150 $W/m^2 \cdot K$ and it was assumed that the cross-sectional flux of air covered a discoidal area of diameter 8 mm around the irradiated skin surface. The protocol was as follows: (1) start laser irradiation on the surface of the skin with a pulse repetition rate of 5 Hz, (2) rise the temperature of the epidermis-dermis interface to $T_{reg} = 45^{\circ}C$ and (3) maintain this temperature for 8 s. The reason for setting $T_{reg} = 45^{\circ}C$ at that particular anatomical location is that fibroblasts present in the extracellular matrix of the dermal layer respond to heat stimulation by producing *de novo* collagen and remodelling the existing collagen network [11,35,36]. In turn, these biochemical and structural alterations of the dermis constituents have a positive effect on the mechanobiology and cosmetic appearance of the skin. The links

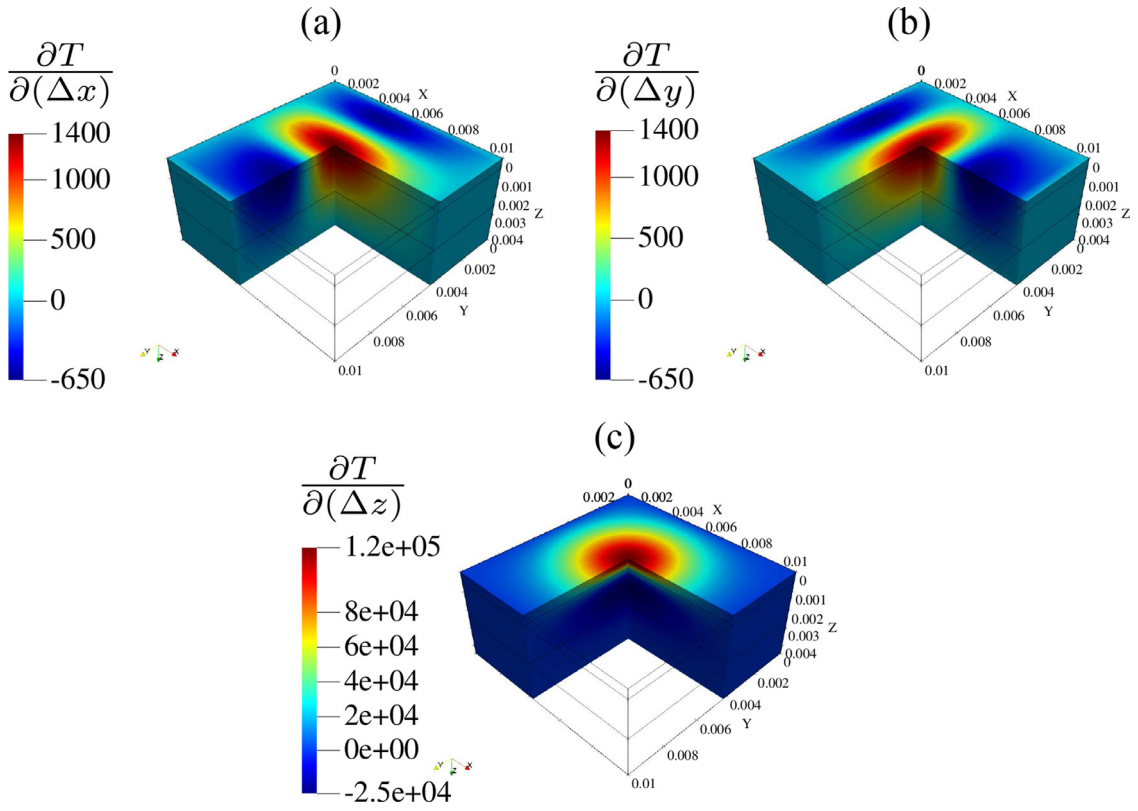

Fig. 10. Temperature sensitivities with respect to spatial steps over the simulation domain. (a)–(c) are the temperature sensitivities with respect to spatial resolution in *x*, *y* and *z*-axis. For the plotted meshes, their spatial resolution were 1, 1 and 0.1 mm, respectively.

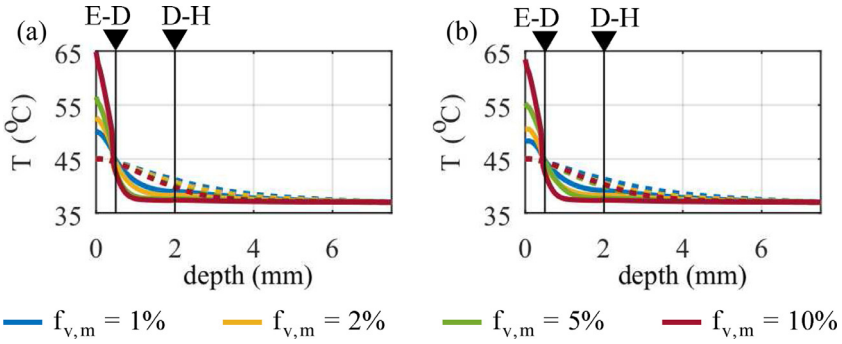

Fig. 11. Temperature distribution inside the skin for different melanin volume fractions $f_{v,m}$ and convective conditions. Temperature T with respect to depth is probed at the geometric centre of the simulated tissue. The solid lines represent the heat distribution at the time when the temperature of the epidermis-dermis interface first reached the desired temperature $T_{reg} = 45°C$. The dashed lines indicate the distribution after maintaining the temperature at 45°C for 8 *s*. E-D and D-H denote the epidermis-dermis and dermis-hypodermis interfaces.

between skin microstructure and its macroscopic mechanical response and appearance are fundamental to many cosmetic treatment strategies and interactions of the skin with engineered devices and consumer products [37–41].

In Fig. 13, eight cases are presented to mimic real skin photorejuvenation treatment scenarios. Fig. 13(a)–(d) shows the cases when the skin was under forced cooling and with melanin volume fractions ranging from 1, 2, 5 to 10%, respectively. Fig. 13(e)–(h) were experiencing the natural convection and their melanin volume fractions were 1, 2, 5 and 10%, respectively. The input time function and temperature evolution of the epidermis-dermis and dermis-hypodermis interfaces with respect to time are reported for each case in Fig. 13. In addition, the dissection of the simulated tissue at two time instances is illustrated in Fig. 13. In the figure, the skin contains higher melanin content from left to right, and it experiences natural and forced cooling from bottom to top. Whilst regulating the temperature at the epidermis-dermis interface, the surface temperature shows an increasing trend as the melanin content increases. For the cases without cooling ($h = 10$ W/m$^2 \cdot$ K) and darker skin tones $f_{v,m} = 5 - 10\%$) in Fig. 13(g) and (h) the surface temperature abruptly increases to 60°C. Temperature spikes lasting less than a second are sufficient to induce pain and burn the skin surface [42].

In Fig. 13(c) and (d), the temperature profiles of the skin tissue under laser irradiation with a controlled cooling are reported. The peaks of temperature profiles are relatively smaller than those calculated for natural convection cases. The forced cooling also increases the time needed to reach the desired regulated temperature, which decreases the damage on the skin tissue and allows the heat to penetrate deeper into the tissue. Fig. 12 shows the time needed to raise the temperature in the epidermis-dermis interface as a function of laser light energy at 45°C for different melanin

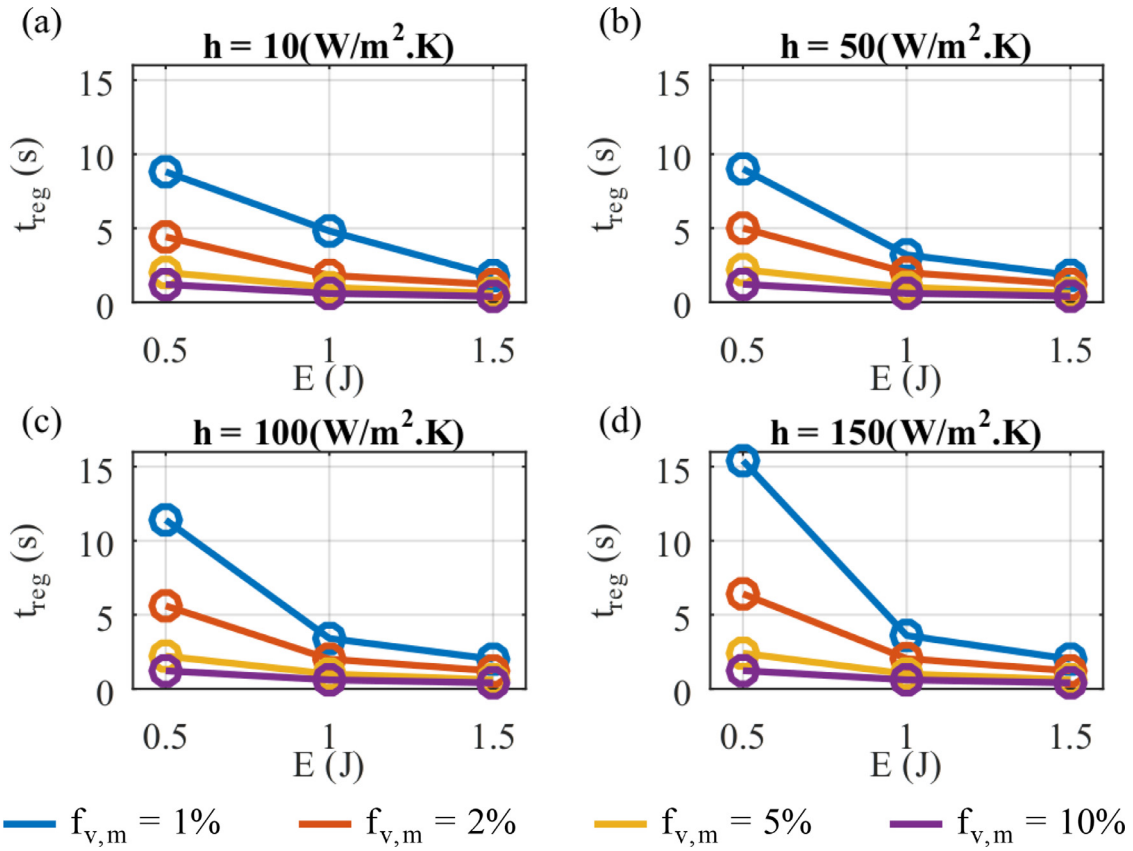

Fig. 12. Time required to reach the temperature in the epidermis-dermis interface with respect to laser energy under different convection conditions (h) and melanin volume fraction ($f_{v,m}$). The plotted data was probed at the geometric centre of the epidermis-dermis interface.

skin content under various cooling conditions. Fig. 11 shows the temperature distribution within the skin for all eight cases considered here.

4.3. Arrhenius damage integral

Quantification of damage in biological tissue is defined as the ratio of concentrations of viable cells before and after temperature rises to a critical level (45°C) in the living tissue. The change in concentration is due to thermal necrosis of cells. Moritz and Henriques [43] defines tissue damage in the context of a rate process model. This model is known as the Arrhenius damage integral.

$$\Omega(x,y,z,t) = \ln\left\{\frac{C(0)}{C(\tau_d)}\right\} = A\int_0^t e^{\left\{-\frac{E_0}{R\ T(x,y,z,t)}\right\}}dt \tag{47}$$

Here, A denotes the frequency factor of molecular collision, E_0 is the activation energy for denaturation, and R is the gas constant. $C(0)$ is the initial concentration of the viable cells and $C(t)$ is the concentration after time t. According to Moritz and Henriques [43], $\Omega = 1$ corresponds to 63% cell viability which is associated with irreversible tissue damage. In this study, we have used Arrhenius damage integral to compute the amount of damage inflicted to the skin during laser light irradiation. Fig. 14 shows the amount of damage that occurred to a skin tissue undergoing laser light at 1064 nm wavelength and 1.5 J energy for 8 – 10 s. In Fig. 14, the damage is plotted with respect to tissue depth for different cooling conditions and volume fractions of melanin. In all cases, Ω is smaller than one, except for the skin tissue with a 10% melanin volume fraction. This trend is consistent with both the cooling conditions simulated in this study. Fig. 15 reports the spatial distribution of damage that occurred in the skin. Skins having a 1, 2 and 5% volume fraction of melanin undergo reversible damage in both convection conditions. However, skin with 10% volume fraction of melanin experiences irreversible damage at its surface. The high absorption of photo-energy of melanin is responsible for this behaviour. As the skin is exposed to laser irradiation for comparatively less duration, damage can only be observed within the epidermis.

5. Discussion

The core purpose of the model presented in this paper was to develop a multiphysics modelling framework for skin thermo-optical behaviour in order to offer a rational and quantitative basis to enable the control of a robotic system for laser photorejuvenation procedures. The correct dosing of thermal stimulation is critical for the safety and success of these treatment procedures. This controlled dosimetry is also known as concurrent thermal dosimetry [44]. To deliver an accurate thermal dose, a mechanistic understanding of the physics of laser irradiation and propagation into skin coupled to thermal effects is a must. The model that was developed to address this requirement accounts for the structuro-physical properties of the skin whilst also being parametrised by the characteristics of the laser treatment (e.g. convection condition, laser wavelength, laser diameter and laser energy). Importantly, this novel model offers the ability to quantify the interplay of optical and thermal phenomena in relations to the structural properties of the skin which is a complex heterogeneous layered assembly. Therefore, compared to similar models found in the literature [3,27,45–51], our model offers a new level of fidelity and captures non-linear feedback mechanisms which are essential in the development of a controlled robotic system.

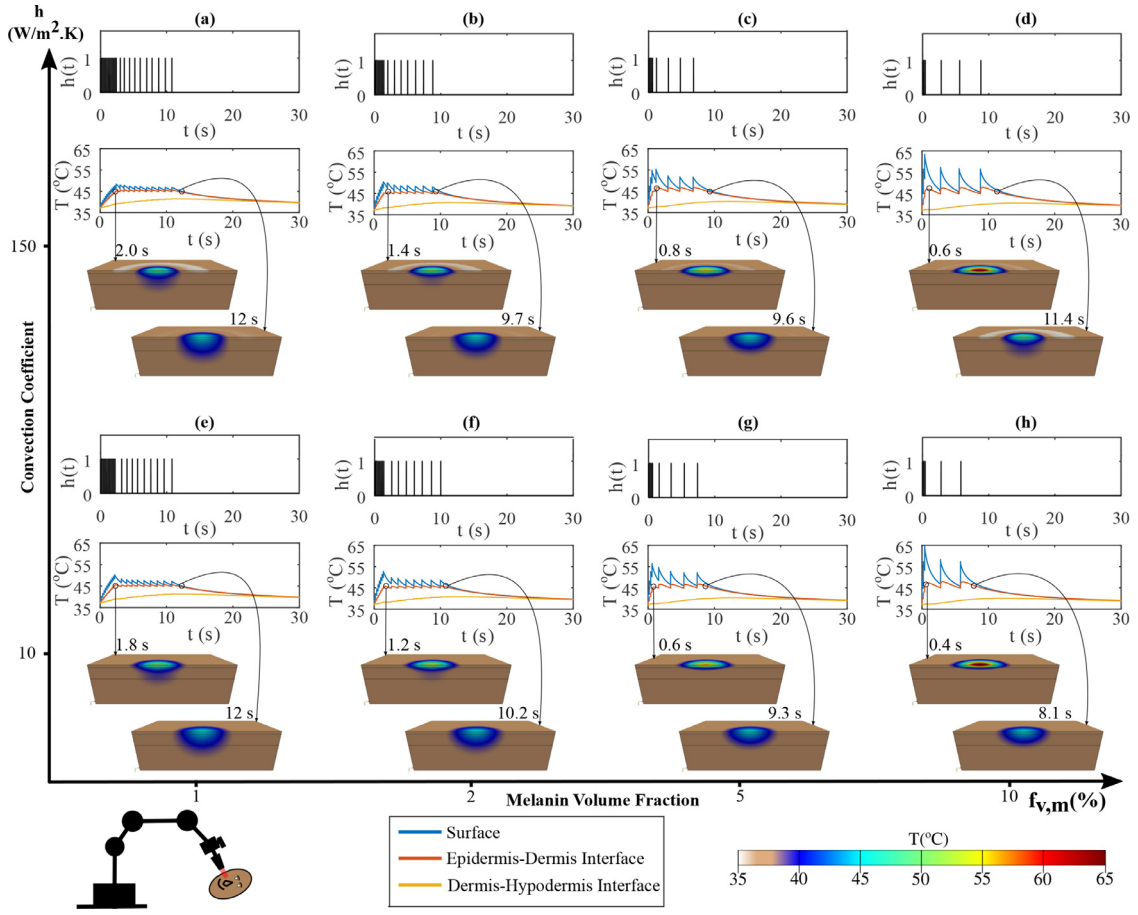

Fig. 13. Eight cases simulating real-life treatment scenarios. Each case is represented by three graphs. The first graph in each case is the impulsive signal with respect to time, which represents the laser irradiation sequence $h(t)$. The second graph reports the temperature with respect to time, which shows-he temperature change on the geometric centre of the skin surface, epidermis-dermis interface and dermis-hypodermis interface after exposing the skin surface to 1064 *nm* pulsed laser light of 1.5 J. The third graph in each case is a dissection of the skin to analyse the heat distribution at two time instances. The first dissection is at the instant when the temperature reaches 45°C at the centre of epidermis-dermis interface. The other is after maintaining the temperature at 45°C for 8 s. All parameters for the 8 simulations were identical except the convection coefficient (h) and the melanin volume fraction ($f_{v,m}$). These two parameters were: (a) $h = 10$ W/m$^2 \cdot$ K, $f_{v,m} = 1\%$. (b) $h = 10$ W/m$^2 \cdot$ K, $f_{v,m} = 2\%$. (c) $h = 10$ W/m$^2 \cdot$ K, $f_{v,m} = 5\%$. (d) $h = 10$ W/m$^2 \cdot$ K, $f_{v,m} = 10\%$. (e) $h = 150$ W/m$^2 \cdot$ K, $f_{v,m} = 1\%$. (f) $h = 150$ W/m$^2 \cdot$ K, $f_{v,m} = 2\%$. (g) $h = 150$ W/m$^2 \cdot$ K, $f_{v,m} = 5\%$. (h) $h = 150$ W/m$^2 \cdot$ K, $f_{v,m} = 10\%$.

The numerical methods and analyses described in this paper were implemented in the general symbolic-numeric software package GNU Octave 6 [52]. The developed code is intended to be used in conjunction with the skin photorejuvenation robot reported in Muddassir et al. [15,16] and the work presented here is a logical progression toward the production of a fully automated robotic system for laser treatment procedures. The behaviour of the mathematical and numerical model was assessed using direct sensitivity analyses against all its constitutive parameters. Sensitivity analyses with respect to only the most influential parameters were reported in Section 4.1. It was observed that the increase in thermal conductivity of the skin decreased the heat deposition in each control volume. This is due to the fact that control volumes can transfer higher heat flux to their neighbouring control volumes when these control volumes have higher thermal conductivities. As expected, the temperature of the epidermis is very sensitive to change in convection conditions. From natural convection ($h = 10$ W/m$^2 \cdot$ K) to forced cooling ($h = 150$ W/m$^2 \cdot$ K), the temperature within the epidermis decreases to 18% and the temperature in the dermis to 9%. For 1064 *nm* wavelength light, skin behaves as a scattering medium. Its absorption coefficient is relatively smaller than the scattering coefficient for this wavelength (e.g. for the skin having melanin volume fraction 1%, the absorption coefficient is 0.66 cm^{-1} and reduced scattering coefficient is 29.1 cm^{-1}). The increase of around 100% in the value of scattering coefficient of dermis caused a decrease in the temperature in the epidermis about 18.25%, 9% in the dermis and 2.25% in the hypodermis. This temperature drop agrees with expected optical behaviour of the dermis, as an increase in the scattering property of a medium reduces its energy absorption capacity.

The proposed numerical method and automatic temperature control, combined with a photorejuvenation robot, can offer a robust and consistent platform to deliver precise thermal stimulation of the skin. However, by definition, the current model has limitations in terms of the physical phenomena and structural effects it accounts for. A more refined model could include the effects of blood vessels density beneath the treated surface, surface curvatures, poroelastic characteristics and surface and heterogeneities within the skin (e.g. hair follicles and sebaceous glands). Metabolic heat generation is also an important factor to consider for the modelling of thermal interactions in biological tissues. Such a source term is not considered in (1) for two reasons: (i) photorejuvenation treatment procedures are performed in a reclined seating position where the metabolic rate is at its lowest [68] and (ii) laser stimulations for these procedures are applied for extremely short durations, thus the cumulative effect of metabolic heat generation can be considered negligible.

Of particular importance, the model presented in this papers considers a spatially-uniform concentration of haemoglobin and melanocytes (i.e. cells that produce melanin) in skin, but in re-

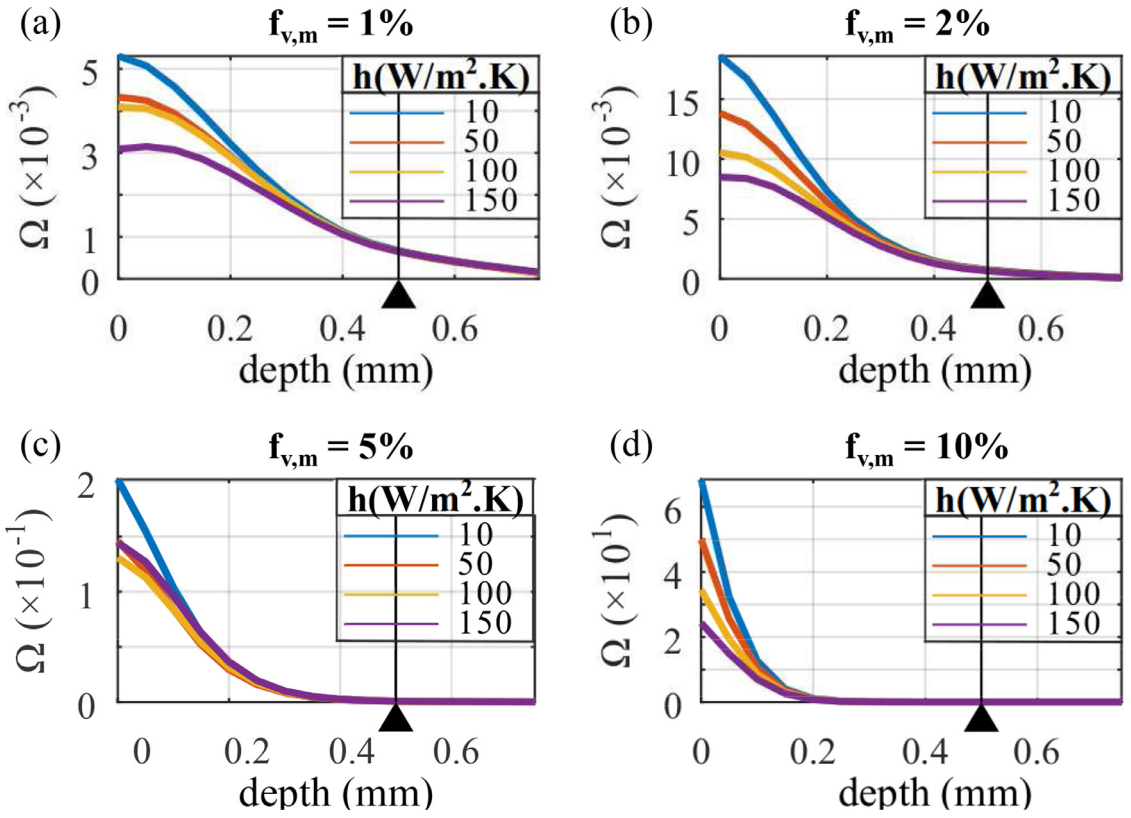

Fig. 14. Amount of tissue damage during laser light irradiation under different convection conditions for various skin tones. The solid black vertical line is the epidermis-dermis interface. ▲ is pointing towards the epidermis-dermis interface. (a)–(d) are the damage-depth plots when the melanin volume fraction $f_{v,m}$ are 1, 2, 5 and 10%, respectively.

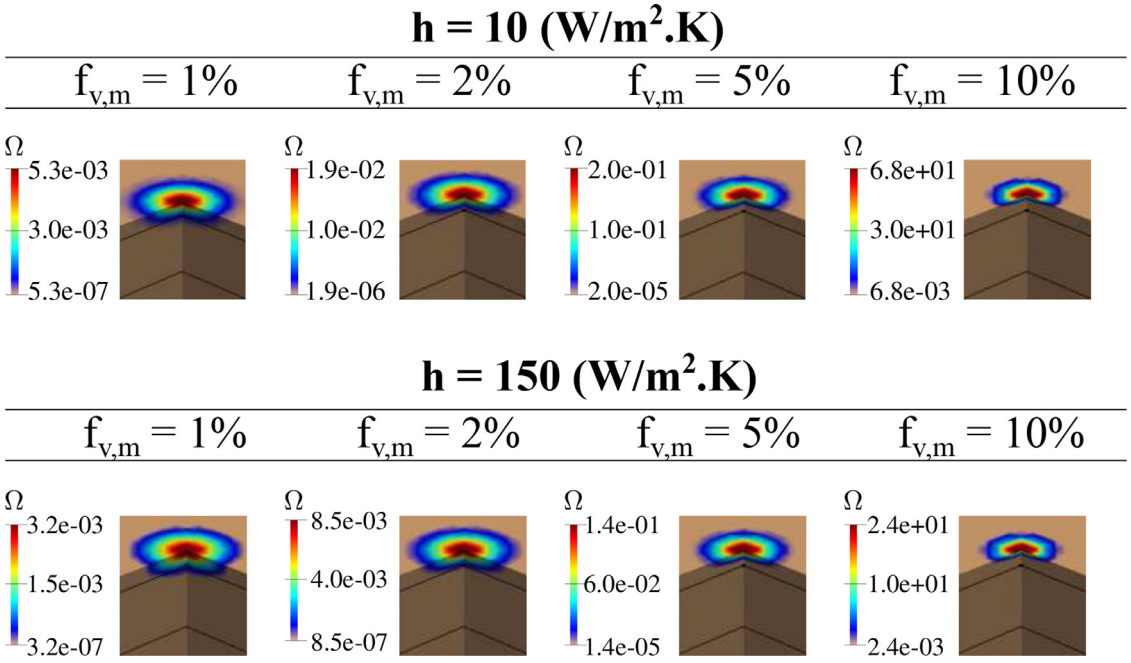

Fig. 15. Distribution of Arrhenius damage. Coloured mesh representation of skin tissue damage after regulating the temperature at 45°C in the epidermis-dermis interface under different cooling conditions and for various volume fractions of melanin ($f_{v,m}$) or skin tones.

ality, this protein and these cells have highly heterogeneous distributions [53]. In all the numerical simulations conducted in the present study a 1064 *nm* laser light was considered. Pigment chromophores, also present in hair follicles, are susceptible to absorb this particular electromagnetic wavelength and therefore also affect heat generation within the tissue. It is easy to realise that any geometric and material perturbation in the skin microstructure has the potential to significantly alter heat generation and distribution. The effects of nevi and lentigo-also correlated with ethnicity [54], like melanin would not be relevant as during rejuvenation treatment procedures areas containing them are treated separately.

As alluded in the previous paragraph, accounting for heterogeneities within the skin whether there are related to tissue microstructure or physical properties, offers the prospect of increasing the biological fidelity and accuracy of our model. Heterogeneities in spatial distribution of biophysical properties could be accounted for by using stochastic finite element techniques [55] which can efficiently represent stochastic fields (i.e. random variables indexed by space) directly in the partial/ordinary differential equations governing the physics of a system.

The effects of thermal expansion due to increase in temperature might also be important to consider.

To enable more flexibility in terms of simulation domain geometry and constitutive behaviour the model presented in this study could be developed further by implementing it into a robust multi-field finite element formulation. This numerical framework would make our current model unsuitable for near real-time computations but would offer the ability to model complex coupled physics problems over unstructured domains of arbitrary complexity under complex Dirichlet and Neumann conditions. Such an off-line simulator could assist in running large scale parametric and optimisation studies, with great accuracy. For example, the finite strain thermo-mechanical finite element formulation for skin of McBride et al. [56] could be used to study contact-based rejuvenation treatments like those based on radio frequency and intense pulsed light (IPL).

Arrhenius damage integral provides a framework to quantify the viability of a tissue subjected to controlled or uncontrolled cell necrosis. In the eight cases analysed in this study, the cell viability in only two cases, with 10% melanin volume fraction, was not ensured (Ω exceeds 1). This suggests that special care is required to select laser energy and intensity for darker skin tones.

Experimental evaluation of photo-thermal skin-laser interactions (e.g. [57]) is needed to validate the presented numerical model. It was found that temperature distributions with respect to time and depth are in line with those of comparable studies [21,27,57,58]. An experimental setup may contain an artificial skin surrogate such as that reported in Chen et al. [59], which can attempt to mimic the thermo-mechanical and optical properties of living tissue and can be fabricated with embedded temperature sensors. Despite our inability to faithfully model the complex physics of skin-laser interactions such an experimental platform would offer the ability to validate the mathematical and numerical models/methods and the control system to be used in driving a photorejuvenation robot. Clinical studies would be conducted in the later stages of this study.

6. Conclusion

In this study, constitutive equations based on the Pennes bioheat equation were developed and numerically implemented using a finite volume method to represent the photo-thermal laser-skin interactions occurring in laser photorejuvenation procedures. A key feature of the model was the capability to simultaneously account for the layer-specific optical and thermal properties of each skin layer whilst also accounting for the external thermal conditions and settings of the laser. Extensive parametric analyses were conducted to assess the performance of the model which demonstrated the pertinence of the biophysical skin parameters and physical parameters of the laser source included in the model. Numerical analyses highlighted significant differences in laser treatment response according to skin type and biophysical properties. The implications of these findings are very important, particularly in the light of the ageing of ethnically-diverse populations as ageing induces degradation of the biophysical properties and physiological functions of the skin [37,60]. Moreover, there is strong evidence of correlations between ethnicity and certain biophysical properties including skin elasticity and tissue composition [61–63]. These facts support the need for developing next-generation biophysical models of skin that would be parametrised by age, ethnicity and also biological sex, so that a new level of biological fidelity could be achieved.

These facts support the need for developing next-generation biophysical models of skin that would be parametrised by age, ethnicity and also biological sex, so that a new level of biological fidelity could be achieved.

The model presented in this paper paves the ways for smart robotic systems for photorejuvenation procedures that are based on predictive biophysics-informed numerical simulations. Ultimately, such systems will offer a viable option for personalised treatment which will improve efficiency, safety and outcome of current treatment procedures.

Declaration of Competing Interest

The authors declare that there is no conflict of interest.

Acknowledgement

This work was supported in part by the Key-Area Research and Development Program of Guangdong Province (2020B090928001), in part by the Research Grants Council under grant 15212721, in part by the Jiangsu Industrial Technology Research Institute Collaborative Funding Scheme under grant K-ZG9V.

Supplementary material

Supplementary material associated with this article can be found, in the online version, at doi:10.1016/j.cmpb.2022.106653.

References

[1] D.J. Goldberg, Hair Removal Using Light-Based Systems, in: Cosmetics Applications of Laser & Light-Based Systems, Elsevier, 2009, pp. 145–156, doi:10.1016/B978-0-8155-1572-2.50010-5.
[2] J.E. Oblong, Wrinkles: cosmetics, drugs, and energy-based systems, in: Cosmetics Applications of Laser & Light-Based Systems, Elsevier, 2009, pp. 301–316, doi:10.1016/B978-0-8155-1572-2.50020-8.
[3] F. Xu, T. Lu, Skin bioheat transfer and skin thermal damage, in: Introduction to Skin Biothermomechanics and Thermal Pain, Springer Berlin Heidelberg, 2011, pp. 23–86.
[4] S.W. Lanigan, Lasers in Dermatology, Springer Science & Business Media, 2000.
[5] M.P. Goldman, R.E. Fitzpatrick, Cutaneous Laser Surgerythe Art and Science of Selective Photothermolysis, Mosby,, 1994.
[6] H. Lui, R.R. Anderson, Radiation sources and interaction with skin, in: H.W. Lim, H. Hönigsmann, J.L.M. Hawk (Eds.), Photodermatology, CRC Press, 2007, pp. 29–40.
[7] S.P. Nistico, M. Silvestri, T. Zingoni, F. Tamburi, L. Bennardo, G. Cannarozzo, Combination of fractional CO_2 laser and rhodamine-intense pulsed light in facial rejuvenation: a randomized controlled trial, Photobiomodulation Photomed. Laser Surg. 39 (2) (2021) 113–117.
[8] A. Capon, S. Mordon, Can thermal lasers promote skin wound healing? Am. J. Clin. Dermatol. 4 (1) (2003) 1–12, doi:10.2165/00128071-200304010-00001.
[9] A.K. Verrico, J.V. Moore, Expression of the collagen-related heat shock protein HSP47 in fibroblasts treated with hyperthermia or photodynamic therapy, Br. J. Cancer 76 (6) (1997) 719–724, doi:10.1038/bjc.1997.452.
[10] A. Verrico, A. Haylett, J. Moore, In vivo expression of the collagen-related heat shock protein HSP47, following hyperthermia or photodynamic therapy, Lasers Med. Sci. 16 (3) (2001) 192–198, doi:10.1007/PL00011354.

[11] S.D. Dams, M. de Liefde-van Beest, A.M. Nuijs, C.W. Oomens, F.P. Baaijens, Pulsed heat shocks enhance procollagen Type I and procollagen Type III expression in human dermal fibroblasts, Skin Res. Technol. 16 (3) (2010) 354–364, doi:10.1111/j.1600-0846.2010.00441.x.
[12] S.D. Dams, M. De Liefde-van Beest, A.M. Nuijs, C.W. Oomens, F.P. Baaijens, Heat shocks enhance procollagen Type I and III expression in fibroblasts in ex vivo human skin, Skin Res. Technol. 17 (2) (2011) 167–180, doi:10.1111/j.1600-0846.2010.00473.x.
[13] J.S. Resneck, A.B. Kimball, Who else is providing care in dermatology practices? Trends in the use of nonphysician clinicians, J. Am. Acad. Dermatol. 58 (2) (2008) 211–216, doi:10.1016/j.jaad.2007.09.032.
[14] J.P. Farkas, J.E. Hoopman, J.M. Kenkel, Five parameters you must understand to master control of your laser/light-based devices, Aesthet. Surg. J. 33 (7) (2013) 1059–1064, doi:10.1177/1090820X13501174.
[15] M. Muddassir, S.U. Chan, D. Gomez, D. Navarro-Alarcon, Can a robot outperform a human operator in skin photorejuvenation? J. Cosmet. Dermatol. 1 (February) (2021) 1–2, doi:10.1111/jocd.14005.
[16] M. Muddassir, D. Gomez, L. Hu, S. Chen, D. Navarro-Alarcon, Robotics meets cosmetic dermatology: development of a novel vision-guided system for skin photo-rejuvenation, IEEE ASME Trans. Mechatron. (2021) 1–11, doi:10.1109/TMECH.2021.3075207.
[17] K.R. Diller, Modeling of bioheat transfer processes, Adv. Heat Transf. 22 (1992) 157–357.
[18] G. Limbert, Mathematical and computational modelling of skin biophysics: a review, Proc. R. Soc. A Math. Phys. Eng. Sci. 473 (2203) (2017) 20170257, doi:10.1098/rspa.2017.0257.
[19] H.K. Graham, A. Eckersley, M. Ozols, K.T. Mellody, M.J. Sherratt, Human skin: composition, structure and visualisation methods, in: G. Limbert (Ed.), Skin Biophysics, 22, Springer International Publishing, Cham, 2019, pp. 1–18, doi:10.1007/978-3-030-13279-8_1.
[20] H.H. Pennes, Analysis of tissue and arterial blood temperatures in the resting human forearm, J. Appl. Physiol. 1 (2) (1948) 93–122, doi:10.1152/jappl.1948.1.2.93. PMID: 18887578
[21] S.L. Jacques, Corrigendum: optical properties of biological tissues: a review, Phys. Med. Biol. 58 (14) (2013) 5007–5008, doi:10.1088/0031-9155/58/14/5007.
[22] S. Alaluf, S. Alaluf, A. Heath, N.I. Carter, D. Atkins, H. Mahalingam, K. Barrett, R.I. Kolb, N. Smit, Variation in melanin content and composition in type V and VI photoexposed and photoprotected human skin: the dominant role of DHI, Pigment Cell Res. 14 (5) (2001) 337–347, doi:10.1034/j.1600-0749.2001.140505.x.
[23] S. Alaluf, D. Atkins, K. Barrett, M. Blount, N. Carter, A. Heath, Ethnic variation in melanin content and composition in photoexposed and photoprotected human skin, Pigment Cell Res. 15 (2) (2002) 112–118, doi:10.1034/j.1600-0749.2002.1o071.x.
[24] M.J. Van Gemert, S.L. Jacques, H.J. Sterenborg, W.M. Star, Skin optics, IEEE Trans. Biomed. Eng. 36 (12) (1989) 1146–1154, doi:10.1109/10.42108.
[25] A.J. Welch, M.J. van Gemert, Overview of optical and thermal laser-tissue interaction and nomenclature, in: Optical-Thermal Response of Laser-Irradiated Tissue, Springer Netherlands, 2010, pp. 3–11.
[26] T. Ždl, P. Togni, L. Víšek, J. Vrba, Comparison of constant and temperature dependent blood perfusion in temperature prediction for superficial hyperthermia, Radioengineering 19 (2) (2010) 281–289.
[27] M. Milanic, B.T. Muc, N. Lukac, M. Lukac, Numerical study of hyper thermic laser lipolysis with 1,064 nm Nd:YAG laser in human subjects, Lasers Surg. Med. 51 (10) (2019) 897–909, doi:10.1002/lsm.23124.
[28] T. Drizdal, P. Togni, L. Visek, J. Vrba, Comparison of constant and temperature dependent blood perfusion in temperature prediction for superficial hyperthermia, Radioengineering 19 (2) (2010) 281–289.
[29] K.F. Riley, M.P. Hobson, S.J. Bence, Mathematical Methods for Physics and Engineering: a Comprehensive Guide, Cambridge University Press, 2006.
[30] R.B. Hetnarski, Finite volume method in heat conduction, in: R.B. Hetnarski (Ed.), Encyclopedia of Thermal Stresses, Springer Netherlands, 2014, pp. 1645–1658.
[31] J.C. Butcher, Numerical differential equation methods, in: Numerical Methods for Ordinary Differential Equations, John Wiley & Sons, Ltd, Chichester, UK, 2016, pp. 55–142.
[32] J. Korelc, P. Wriggers, Automation of sensitivity analysis, in: Automation of Finite Element Methods, Springer International Publishing, 2016, pp. 255–309.
[33] J. Korelc, Automation of primal and sensitivity analysis of transient coupled problems, Comput. Mech. 44 (5) (2009) 631–649, doi:10.1007/s00466-009-0395-2.
[34] P. Hasgall, F. Di Gennaro, C. Baumgartner, E. Neufeld, M. Gosselin, D. Payne, A. Klingenböck, N. Kuster, It is database for thermal and electromagnetic parameters of biological tissues, Version 3.0 (2015).
[35] D. Scieglinska, Z. Krawczyk, D.R. Sojka, A. Gogler-Pigłowska, Heat shock proteins in the physiology and pathophysiology of epidermal keratinocytes, Cell Stress Chaperones 24 (6) (2019) 1027–1044, doi:10.1007/s12192-019-01044-5.
[36] T.R. Dafforn, M. Della, A.D. Miller, The molecular interactions of heat shock protein 47 (Hsp47) and their implications for collagen biosynthesis, J. Biol. Chem. 276 (52) (2001) 49310–49319, doi:10.1074/jbc.M108896200.
[37] G. Limbert, M.A. Masen, D. Pond, H.K. Graham, M.J. Sherratt, R. Jobanputra, A. McBride, Biotribology of the ageing skin why we should care, Biotribology 17 (2019) 75–90, doi:10.1016/j.biotri.2019.03.001.
[38] G. Limbert, Investigating the influence of relative humidity on expression microwrinkles, J. Aesthet. Nurs. 7 (4) (2018) 204–207, doi:10.12968/joan.2018.7.4.204.
[39] D. Pond, A. McBride, L. Davids, B. Reddy, G. Limbert, Microstructurally-based constitutive modelling of the skin linking intrinsic ageing to microstructural parameters, J. Theor. Biol. 444 (2018) 108–123, doi:10.1016/j.jtbi.2018.01.014.
[40] G. Limbert, E. Kuhl, On skin microrelief and the emergence of expression micro-wrinkles, Soft Matter 14 (8) (2018) 1292–1300, doi:10.1039/C7SM01969F.
[41] M.F. Leyva-Mendivil, J. Lengiewicz, A. Page, N.W. Bressloff, G. Limbert, Skin microstructure is a key contributor to its friction behaviour, Tribol. Lett. 65 (1) (2017) 12, doi:10.1007/s11249-016-0794-4.
[42] F. Xu, T. Lu, Physiological features of pain sensation, in: Introduction to Skin Biothermomechanics and Thermal Pain, Springer Berlin Heidelberg, 2011, pp. 343–373.
[43] A.R. Moritz, F.C. Henriques Jr, Studies of thermal injury, Am. J. Pathol. (1946) 530–549.
[44] R.B. Roemer, Thermal dosimetry, in: Thermal Dosimetry and Treatment Planning, Springer Berlin Heidelberg, 1990, pp. 119–208.
[45] C.K. Charny, Mathematical models of bioheat transfer, in: Y.I. Cho (Ed.), Bioengineering Heat Transfer, Adv. Heat Transf., 22, Elsevier, 1992, pp. 19–155.
[46] K. Kim, Z. Guo, Multi-time-scale heat transfer modeling of turbid tissues exposed to short-pulsed irradiations, Comput. Methods Programs Biomed. 86 (2) (2007) 112–123, doi:10.1016/j.cmpb.2007.01.009.
[47] S.R. Mordon, B. Wassmer, J. Reynaud, J. Zemmouri, Mathematical modeling of laser lipolysis, Biomed. Eng. Online 7 (1) (2008) 10, doi:10.1186/1475-925X-7-10.
[48] J. Zhou, J. Liu, Numerical study on 3-D light and heat transport in biological tissues embedded with large blood vessels during laser-induced thermotherapy, Numer. Heat Transf. Part A Appl. 45 (5) (2004) 415–449.
[49] K. Chen, Y. Liang, W. Zhu, X. Sun, T. Wang, Simulation of temperature distribution in skin under laser irradiation with different wavelengths, Optik 125 (5) (2014) 1676–1679.
[50] M. Milanic, A. Cenian, N. Verdel, W. Cenian, J. Stergar, B. Majaron, Temperature depth profiles induced in human skin in vivo using pulsed 975 nm irradiation, Lasers Surg. Med. 51 (9) (2019) 774–784.
[51] D.A. Hodson, J.C. Barbenel, G. Eason, Modelling transient heat transfer through the skin and a contact material, Phys. Med. Biol. 34 (10) (1989) 1493–1507.
[52] J.W. Eaton, D. Bateman, S. Hauberg, R. Wehbring, GNU octave version 6.1.0 manual: a high-level interactive language for numerical computations, 2020.
[53] S. Cotton, E. Claridge, Developing a predictive model of human skin coloring, in: R.L. Van Metter, J. Beutel (Eds.), Imaging, 2708, 1996, pp. 814–825.
[54] L.A. Crane, S.T. Mokrohisky, R.P. Dellavalle, N.L. Asdigian, J. Aalborg, T.E. Byers, C. Zeng, A.E. Barn, J.M. Burch, J.G. Morelli, Melanocytic nevus development in Colorado children born in 1998: a longitudinal study, Arch. Dermatol. 145 (2) (2009) 148–156.
[55] G. Stefanou, The stochastic finite element method: past, present and future, Comput. Methods Appl. Mech. Eng. 198 (2009) 1031–1051.
[56] A. McBride, S. Bargmann, D. Pond, G. Limbert, Thermoelastic modelling of the skin at finite deformations, J. Therm. Biol 62 (2016) 201–209, doi:10.1016/j.jtherbio.2016.06.017.
[57] C. Sturesson, S. Andersson-Engels, A mathematical model for predicting the temperature distribution in laser-induced hyperthermia. Experimental evaluation and applications, Phys. Med. Biol. 40 (12) (1995) 2037–2052, doi:10.1088/0031-9155/40/12/003.
[58] M.J. Van Gemert, S.L. Jacques, H.J. Sterenborg, W.M. Star, Skin optics, IEEE Trans. Biomed. Eng. 36 (12) (1989) 1146–1154, doi:10.1109/10.42108.
[59] A.I. Chen, M.L. Balter, M.I. Chen, D. Gross, S.K. Alam, T.J. Maguire, M.L. Yarmush, Multilayered tissue mimicking skin and vessel phantoms with tunable mechanical, optical, and acoustic properties, Med. Phys. 43 (6Part1) (2016) 3117–3131, doi:10.1118/1.4951729.
[60] D.J. Tobin, Introduction to skin aging, J. Tissue Viability 26 (1) (2017) 37–46, doi:10.1016/j.jtv.2016.03.002.
[61] N.O. Wesley, H.I. Maibach, Racial (Ethnic) differences in skin properties: the objective data, Am. J. Clin. Dermatol. 4 (12) (2003) 843–860.
[62] A. Langton, M. Sherratt, W. Sellers, C. Griffiths, R. Watson, Geographical ancestry is a key determinant of epidermal morphology and dermal composition, Br. J. Dermatol. 171 (2) (2014) 274–282.
[63] A. Langton, H. Graham, J. McConnell, M. Sherratt, C. Griffiths, R. Watson, Organization of the dermal matrix impacts the biomechanical properties of skin, Br. J. Dermatol. 177 (3) (2017) 818–827.
[64] C. W. Song, H. J. Park, C. K. Lee, R. Griffin, Implicationsof increased tumor blood flow and oxygenation caused by mildtemperature hyperthermia in tumor treatment, Int. J. Hyperthermia 21 (8) (2005) 761–767.
[65] S. Alekseev, M. Ziskin, Human skin permittivity determinedby millimeter wave reflection measurements, Bioelectromagnetics 28 (5) (2007) 331–339.
[66] Y. Lee, K. Hwang, Skin thickness of Korean adults, Surg. Radiol. Anat. 24 (3-4) (2002) 183–189.
[67] K. Hoffmann, M. Stuucker, T. Dirschka, S. Goortz, S. El-Gammal, K. Dirting, A. Hoffmann, P. Altmeyer, Twenty MHz B-scan sonography for visualization and skin thickness measurement ofhuman skin, J. Eur. Acad. Dermatol. Venereol. 3 (3) (Aug. 1994) 302–313.
[68] "Met - Metabolic Rate." [Online]. Available: https://www.engineeringtoolbox.com/met-metabolic-rate-d733.html.